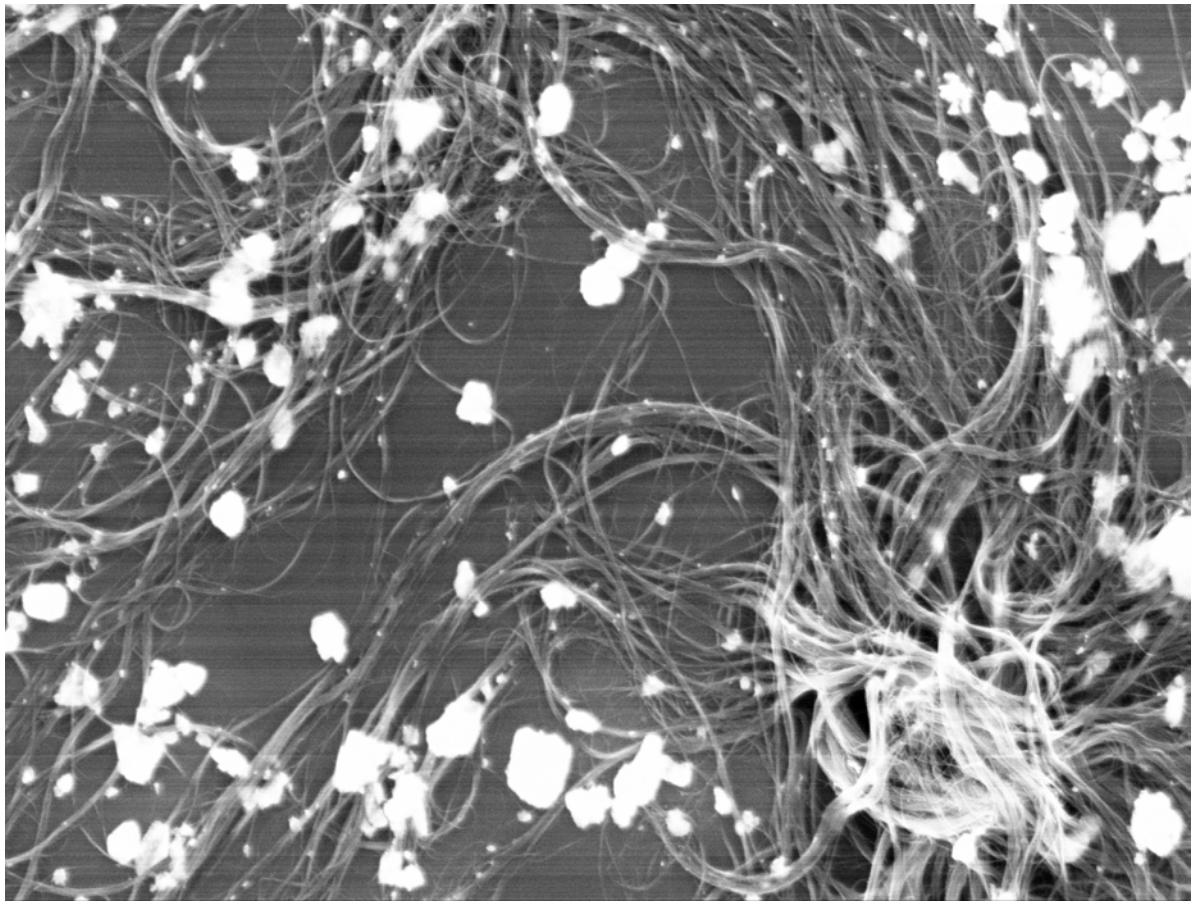


CHALMERS
UNIVERSITY OF TECHNOLOGY



Carbon Nanotube Networks as Thermally Conducting Layers

Master's thesis in Nanotechnology

DAVID JUTERÄNG

Department of Microtechnology and Nanoscience
CHALMERS UNIVERSITY OF TECHNOLOGY
Gothenburg, Sweden 2022

Master's thesis 2022

Carbon Nanotube Networks as Thermally Conducting Layers

DAVID JUTERÄNG



CHALMERS
UNIVERSITY OF TECHNOLOGY

Department of Microtechnology and Nanoscience
MC2
Electronics Materials and Systems Laboratory
Chalmers University of Technology
Gothenburg, Sweden 2022

Carbon Nanotube Networks as Thermally Conducting Layers
DAVID JUTERÄNG

© DAVID JUTERÄNG, 2022.

Supervisor: Yifeng Fu, Department of Microtechnology and Nanoscience
Examiner: Johan Liu, Department of Microtechnology and Nanoscience

Master's Thesis 2022
Department of Microstechnology and Nanoscience
MC2
Electronics Materials and Systems Laboratory
Chalmers University of Technology
SE-412 96 Gothenburg
Telephone +46 31 772 1000

This work was performed for the Electronics Materials and Systems Laboratory at the department of Microtechnology and Nanoscience.

Cover: SEM scan of Ni/CNT network on Si wafer.

Typeset in LaTeX
Printed by Chalmers Reproservice
Gothenburg, Sweden 2022

Carbon Nanotube Networks as Thermally Conducting Layers.
David Juteräng
Department of Microtechnology and Nanoscience
Chalmers University of Technology

Abstract

Flexible and thermally conductive materials with microfabricated structures are important in a number of different research fields. Different approaches for integration of such materials into functioning devices have been implemented in a plethora of ways. Carbon nanotube networks have been the subject of many studies due to their remarkable physical properties, including high thermal conductivity, high electron mobility, high Young's modulus and their flexibility, but challenges still remain. One hurdle to overcome is the lack of efficient bonds between nanotubes in meshes. In this project, the viability of a nickel/carbon nanotube network have been investigated in the context of a potential thermal spreading hybrid material.

Carbon nanotubes of with different lengths were grown on silicon substrates, dispersed in acetone and mixed into solutions containing Nickel-oxide particles. The blends were deposited onto new Silicon substrates where they formed networks. The Nickel particles stuck to strands and bundles of nanotubes, forming bridges between them. Thermal treatment of the networks were performed at different time scales in order to study the effects of annealing on the networks. The characteristics of the Ni/CNT networks were finally investigated using scanning electron microscopy and Raman spectroscopy in order to study potential changes within them. An increase of the D-peak/G-peak intensity ratio corresponding to longer thermal treatment of the substrates were concluded to be a plausible indicator of increased bonding between the Ni-particles and CNTs.

In addition, a simulation was made of a CNT-CNT electron tunneling junction. This was done in order to provide the theoretical backround for the challenges regarding CNT meshes. The lack of chemical bonds between tubes were calculated to increase the resistance of a square CNT thin film by approximately 150%.

Keywords: CNT, Ni, Thin film, Network, Mesh, Hybrid material, Thermal Conductance, Tunneling, Junction, Raman spectroscopy.

Acknowledgements

I would like to thank Aniruddha Paul for showing me the hands on methods of the Black Magick 1 system. This allowed me to learn the practical approach for growing CNTs in a shorter time than I would have done on my own.

Due to unfortunate external circumstances I could not learn and perform the Raman spectroscopy in this project by myself, as was the original plan. However, with the very generous help of Katarina Logg, the measurements of the substrates could still be made.

This work was performed in part at the Chalmers Material Analysis Laboratory, CMAL. The majority of this work was performed in the Myfab Nanofabrication Laboratory cleanroom.

David Juteräng, Gothenburg, 03 2022

Contents

List of Figures **xi**

List of Tables **xiii**

1 Introduction **1**
1.1 Background . . . 1
1.1.1 Ultra-thin Thermal Conductors . . . 1
1.1.2 Carbon Nanotube Films . . . 2
1.2 Aim . . . 3
1.3 Goals . . . 3
1.4 Limitations . . . 3
1.5 Thesis Report Outline . . . 3

2 Theory **5**
2.1 Carbon Sheet Materials . . . 5
2.1.1 Graphene . . . 5
2.1.2 Carbon Nanotubes . . . 6
2.2 Properties of Carbon Nanotubes . . . 7
2.2.1 Electric Conductivity . . . 7
2.2.2 Mechanical Properties . . . 9
2.2.3 Thermal Properties . . . 9
2.3 CNT Fabrication . . . 11
2.4 Networks of Carbon Nanotubes . . . 11
2.4.1 Bonding Between Tubes . . . 11
2.4.2 Basic CNT Network Thin Films . . . 13
2.4.2.1 Electrical and Optical Properties . . . 13
2.4.2.2 Mechanical and Thermal Properties . . . 13
2.4.3 Improved Characteristics . . . 14
2.4.3.1 Chemically Bonded CNTs . . . 14
2.4.3.2 Doped CNT Networks . . . 14
2.4.3.3 Particle Bridges as an Alternative . . . 15
2.5 The Ineffectiveness of Tunneling . . . 15

3 Methods **17**
3.1 Carbon Nanotube Growth . . . 17
3.1.1 Substrate Preparation . . . 17
3.1.2 Chemical Vapour Deposition . . . 17

3.2 Formation of Nanotube Network . . . 17
3.2.1 Solution Preparation . . . 18
3.2.2 Deposition . . . 19
3.2.2.1 Drop Coating . . . 19
3.2.2.2 Spin Coating . . . 19
3.2.3 Annealing . . . 19
3.3 Characterization Techniques . . . 20
3.3.1 Scanning Electron Microscopy . . . 20
3.3.2 Raman Spectroscopy . . . 21
3.4 Simulating a CNT-CNT Tunneling Junction . . . 22
3.4.1 Probability Functions . . . 24
3.4.2 Tunneling Probability . . . 26
3.4.3 Conditions and parameters . . . 27

4 Results **29**
4.1 Carbon Nanotube Array . . . 29
4.2 Ni and CNT Solution . . . 30
4.3 Networks . . . 30
4.3.1 Iterative Optimization . . . 30
4.3.2 Thermally Treated Optimized Networks . . . 31
4.3.2.1 Optical Investigation . . . 32
4.3.2.2 SEM Investigation . . . 33
4.3.2.3 Raman Spectroscopy . . . 34
4.4 Simulation Output . . . 38
4.4.1 Junction Visualization . . . 38
4.4.2 Calculated Tunneling Resistance . . . 38

5 Conclusion **41**
5.1 Result Discussion . . . 41
5.2 Lessons Learned . . . 42
5.3 Further Research . . . 42

Bibliography **45**

A Appendix 1 **I**

B Appendix 2 **XIII**

C Appendix 3 **XV**

D Appendix 4 **XVII**

E Appendix 5 **XIX**

List of Figures

2.1 Illustration of the pattern of graphene, visualized in two different ways. 5
2.2 Unit cell and energy bands of graphene. 6
2.3 Rounded honeycomb pattern overlaid on a circular chimney. 7
2.4 Description of CNT structure using the notation (n,m). 8
2.5 CNT thermal conductivity 10
2.6 Graphic listing of different CNT fabrication methods. 11
2.7 Seperate CNT tubes fused together. 12
2.8 Crossing CNTs with VdW-interaction 12

3.1 Aixtron Black Magic 1 18
3.2 SEM installation 20
3.3 Raman shift spectra of carbon structures 22
3.4 WITec alpha300 R 23
3.5 Geometry of the simulated CNT-CNT junction. 23
3.6 Energy levels of the tunneling electrons. 25
3.7 Probability functions for the junction. 26
3.8 Interpolated tunneling probability. 27
3.9 Probability and position matrices. 28

4.1 Substrates with CVD-grown CNTs 29
4.2 Grown CNTs of different lengths 30
4.3 Baseline solutions 30
4.4 Comparison with alternatives 31
4.5 Optical images of annealed samples. 32
4.6 SEM images of annealed samples. 33
4.7 Mean Raman spectra of annealed networks. 34
4.8 Comparison of the mean Raman spectra. 35
4.9 Close-up of peaks 35
4.10 Ratio indicating honeycomb lattice quality 36
4.11 D peak height of samples 37
4.12 Probability map of electron position in junction. 38
4.13 Idealized structure of CNT network resistance junctions. 39

5.1 Visualization of an CNT/Ni-particle interaction 41

List of Tables

1.1 Bulk CNT threshold voltage compared to other potential electron emission materials. 1

2.1 Comparison of thermal conductivity. 10

3.1 Thermal treatment of substrates. 19
3.2 Simulation input values. 24

1
Introduction

1.1 Background

1.1.1 Ultra-thin Thermal Conductors

Micro-scale devices are at present fabricated in a plethora of ways for a multitude of markets. The evolution of production methods are constantly pushed forwards, improving the performance of various device aspects. For a significant subgroup of devices, for example electronic or thermal microsystems, there are currently a widespread interest in how to take advantage of the properties of graphene, carbon nanotubes (CNTs) and other 2D-structured materials (Dresselhaus et. al. 2001:preface) [1].

An example of an interesting CNT property is the field emission threshold voltage. This value is of importance in vacuum microelectronics when electronic emission rather than thermionic emission is used to propel charge carriers. The threshold voltage of different bulk materials are listed in table 1.1, where networks of single-walled carbon nanotubes (SWCNTs) is seen to have a lower threshold than alternate materials. This is one of the sought after properties of the electron emitters, along with stability at high current densities. (Dresselhaus et. al. 2001:395) [1].

Table 1.1: Bulk CNT threshold voltage compared to other potential electron emission materials.
The table is a slightly reworded version of a corresponding table found in reference [1].

Emission Material	Threshold for electric field
Mo tips	50-100 V/μm
Si tips	50-100 V/μm
p-type semiconducting diamond	130 V/μm
undoped, defective CVD diamond	30-120 V/μm
amorphous diamond	20-40 V/μm
Cs-coated diamond	20-30 V/μm
graphite power, d $<$ 1 mm	17 V/μm
nanostructured, heat treated diamond	3-5 V/μm
network of SWCNTs	1-3 V/μm

Note that the thickness of a 2D carbon structure is hard to quantify, and as such, different values of investigated properties might be retrieved for individual molecules,

depending on the assumptions made. As an example, one method is to set the thickness of graphene to the spacing of graphite layers (Dresselhaus et. al. 2001:290) [1]. In contrast, when measuring properties of the corresponding bulk materials, the height of the thin film itself is used as thickness, which circumvents the need for any assumptive thickness definition.

As noted above, graphene and CNTs would make competitive alternatives to other thin film conductors on paper. However, using graphene and CNTs in devices yields practical drawbacks and challenges. For instance, even though graphene often is described as transparent, a one layer suspended graphene sheet absorbs as much as 2.3% of incoming white light (Nair, R. R. et al. 2008) [2]. Additional layers drastically increases opacity, which will be discussed in section 2.4.2.1. Meanwhile, the conducting quality of a single CNT does not translate into an equivalent property when collecting a swath of them into a thin-film. Poor electrical connection between the tubes result in lacking performances for films with a current lead through them.

1.1.2 Carbon Nanotube Films

For many devices, functioning CNT network thin films would be advantageous in several ways. However, there are obstacles to overcome in order to achieve such networks that are competitive. This duality are summed up below by two quotes from the European Community Research and Development Information Service, or CORDIS.

- "Carbon nanotubes (CNTs) are, as their name suggests, hollow cylinders with nano-scale diameters (scale of single atoms and molecules) formed from carbon. They have unique properties that make them particularly attractive to the electronics industry. These include very high strength and conductivity and the ability to pack it all into a very small space." (CORDIS 2012) [3]

- "CNTs form networks that can be transparent. In addition, the networks are flexible making it possible to employ them on plastic substrates. Transparent, conductive CNT networks are in their infancy and performance is below expectation in large part due to non-homogeneous tube types in the same sample, impurities, defective tubes and interconnection problems." (CORDIS 2012) [3]

As stated in these quotes, there are several issues to overcome when trying to benefit from the properties of thin film CNT networks in devices. Even though CORDIS focuses mainly on electrical aspects of CNT networks here, the same electron bond structure of the tubes also facilitates heat spreading in the molecules. In the same manner, inter-tube heat spreading is one of the problems that can be addressed when trying to improve thermal conductivity performance.

1.2 Aim

The expectations of the project work has been to investigate the structure of Ni/CNT networks in relation to their fabrication process. This to find the fabrication steps needed to obtain meshes of desired configuration with regard to different uses down the line.

1.3 Goals

The project have four main facets:

1. Determining the parameters needed to obtain suitable CNT networks with Ni-particles as intersections.

2. Investigating the possible formation of carbon structures on the surface of the Ni-intersections.

3. Achieving self-sufficiency in fabricating and characterizing networks.

4. Summarizing the opportunities and challenges of Ni/CNT networks based on practical experience obtained according to the points above.

Due to the unpredictable nature of the self-assembly of the networks, approximate and step-wise inspections of the process has been performed rather than specifying distinct initial values. In true trial-and-error fashion, rough estimates from inspection of the network details was used as a guide for subsequent fabrication attempts.

1.4 Limitations

As the project focuses on the production steps of an Ni/CNT matrix with various potential uses, measurements of mechanical and electrical properties of the fabricated networks was not included in the project parameter. Furthermore, SEM and RAMAN spectroscopy was used to investigate the network material and substrates that underwent thermal treatment, but additional investigation by for example TEM would have been beneficial in the assertion of the project conclusions. This was however deemed to be outside the scope of the project.

1.5 Thesis Report Outline

The theory chapter begins with an overview of graphene and the cause of the material's properties. An outline of the correspondence between graphene and CNTs is provided, after which research advances in the field of CNT thin film networks is discussed.

Applied techniques and equipment used are described in the Methods Chapter. The work flow and particulars of the individual tasks are provided along with general explanations of what happens on the molecular level. Also, a description of how a simulation of a CNT-CNT electron junction is presented here.

A summary of experimental measurements in the Result chapter shown the outcomes of the project workflow. The CNT growth, the solutions that were mixed and the SEM images of the substrates are presented in a concise and structured manner along with the results from the Raman spectroscopy. Simulation results and how they relate to the idea of the project are layed out here as well.

The report closes with the Conclusions chapter. Here, the predictions, result and lessons learned are summarized. Also, an outlook regarding further investigation on the topic is given.

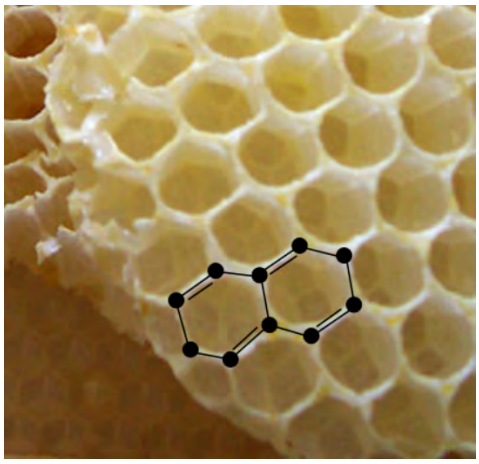
2

Theory

2.1 Carbon Sheet Materials

2.1.1 Graphene

Graphene consists of carbon atoms that are arranged at the corners of a planar hexagon pattern. This pattern occurs in a multitude of everyday objects like chicken wire, cores in sandwich panels and honeycombs. This type of pattern is indeed most often called honeycomb pattern, as shown in figure 2.1a. Since it is the vertices that are the locations of the atoms, it might be easier to visualize the pattern as a stack of balls or cans where the third tile of every row is removed 2.1b. One could consider multiple such carbon molecules layered on top of each other to be graphene as well, but there is not a defined number of layers at which the structure would be considered graphite rather than multi-layered graphene.



(a) Part of a honeycomb with a matching subsection of an atomic pattern. (Wikipedia 2007) [4]



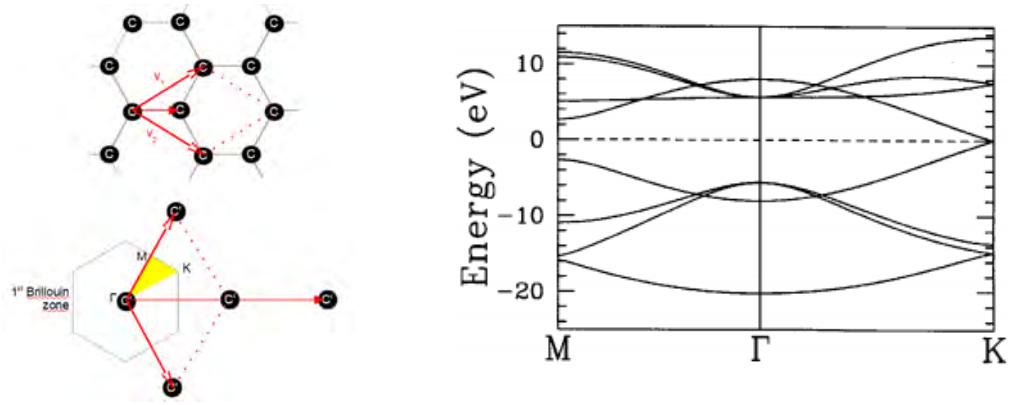
(b) Stack of cans in the pattern of graphene atoms. In each layer, every third can is removed.

Figure 2.1: Illustration of the pattern of graphene, visualized in two different ways.

Each carbon atom in the grid has four valence electrons. Due to the two-dimensional nature of a graphene molecule, each atom only have three neighbours, which means that there are π-bonds formed at every third bond location. These π-bonds does not have fixed locations in the lattice, but are free to move, and therefore electrical currents can be lead through the molecule. How easily an electron can move through

a material depends on the structure of the atoms. To understand the conducting properties of crystals, electronic band structures are calculated in different directions of the crystal. Bands are collections of closely distributed energy levels that the electron can have when being transported in different directions.

To obtain the energy bands of materials, the single electron Schrodinger equation is solved for a periodic potential. The result can be expressed with Bloch waves, which are planar wave functions modified by a periodic function. They are written as $\psi_n(\mathbf{r}) = e^{i\mathbf{kr}} f_n(\mathbf{r})$, where k is the wave vector. For graphene, the solution results in energy bands that are shown in figure 2.2b. The three denoted points of interest in reciprocal space are illustrated in figure 2.2a and it is the boundary lines between them that corresponds to the segments of the band diagram.



(a) **(b)**

Figure 2.2: Unit cell and energy bands of graphene.
(a) Regular and reciprocal unit cell. Γ, M and K are points of special interest in the 1st Brioullin zone. (b) Energy bands for the boundary lines between the points Γ, M and K (Dresselhaus et. al. 2001:116) [1].

Usually, the energy of an electron wave would be proportional to the square of the momentum. For graphene, linear behaviour is found in the vicinity of K. This phenomenon is otherwise observed for particles without mass, such as photons. Because of this, it is often stated that electrons with certain momentum in specific directions move through graphene as if they were without mass.

2.1.2 Carbon Nanotubes

The theoretical graphene formation, like other crystalline structures, does not exist as perfect physical molecules. Real graphene is not infinite, but have boundaries. Also, it is slightly crumpled up rather than existing strictly in a single plane, regardless if it is free-floating or on a substrate. It also bends easily and can be folded unto itself. Although not made by actually folding graphene, one possible structure of bent graphene is the carbon nanotube (CNT), which essentially is a finite strip of graphene where two edges meet each other. The π-bonds and the pattern are otherwise identical. The difference is the curved surface and the periodic boundary

condition in one dimension. Just as the pattern of graphene was similar to that of a stack of cans, the CNT pattern is similar to a round brick chimney, as illustrated in 2.3. Due to the commonality with graphene, the CNT retains many of the inherent characteristics of the two-dimensional structure.

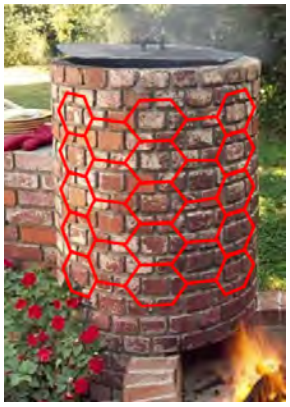


Figure 2.3: Rounded honeycomb pattern overlaid on a circular chimney.
Original image by E. Andrew McKinney (This Old House 2021)[5].

One geometrically dependent difference between a CNT and a corresponding strip of graphene (of the same size, meaning the same length and mass) are the load paths when subjected to forces. For example, in a nanotube, the reaction to a bending force is compression and tension loads in the walls, which are far from the symmetry plane. In contrast, all reaction loads of a graphene strip occurs at the center line. This is basically the same difference as between a rolled up paper and the original sheet. Even though this is a clear mechanical difference between the two structures, it is diffucult to compare straightforward strength values of the molecules, since they are so strong yet hard to handle (Dresselhaus et. al. 2001:298-299) [1].

2.2 Properties of Carbon Nanotubes

2.2.1 Electric Conductivity

The electrical resistance of a CNT is due to a multitude of factors. Besides the direct parameters of diameter and length of the tube, along with possible dopants and impurities, the chirality of the tube plays a significant role as well. As discussed in section 2.1.1, graphene shows different conductivity in different directions of current. Since the CNT has the same pattern as a rolled up graphene sheet, those directional differences come into play here as well.

A rigorous method of classifying CNTs is to map the structure of the tube onto a pattern of graphene and describe it using vectors. In practice, it can be considered as a graphene nanoribbon that has been rolled up with the long edges bonded to each other. In figure 2.4, (n,m) vectors describing a nanotube are illustrated. The pair of vector values result in different diameters of three tube subgroups: armchair, zig-zag and chiral. Zig-zag and armchair tubes have chains of atoms wrapping around end

to end along the tube. The chiral ones does not, resulting in spirals of carbon chains along the length of the tube.

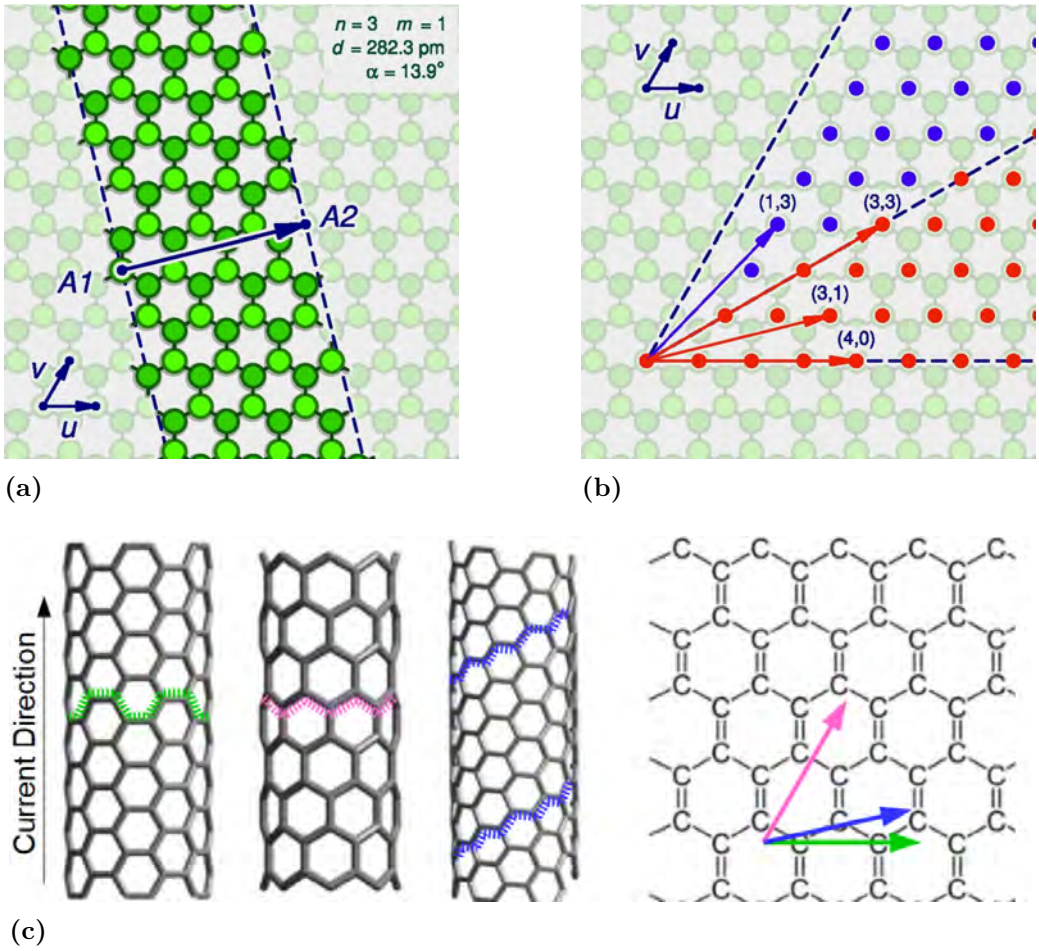


Figure 2.4: Description of CNT structure using the notation (n,m) (Wikipedia 2021) [6].
(a) Boundary condition. v and u are unit vectors defining A2-A1. The example here corresponds to (3,1) in image b. (b) Possible A2-A1 boundary condition vectors in (n,m) notation. Note that zig-zag, armchair and chiral tubes corresponds to values of $n = 0$, $m = n$ and $m \neq n \neq 0$ respectively. (c) The three types of repeating boundary conditions, (armchair, zig-zag and chiral) and their corresponding current directions in the plane (University of Rome Tor Vergata) [7].

The periodicity of a CNT determines if the allowed k-vectors of electrons coincides with the K point of the brillouin zone or not. This difference in pattern in conjunction with the diameter of the tube impacts the electric nature along the length of an individual CNT. Generally speaking, for large diameters, armchair tubes ($m = n$) have metallic conductance with a non-zero bandgap structure. Some zig-zag tubes, along with other configurations where $n - m$ is a multiple of 3, would be semiconductors with a low value band gap. However, due to the curvature of the structure, these are metallic in practice at room temperature. Remaining configurations are

semi-conducting along the tube axis.

Now, if the CNT has a small diameter, hybridization of π and σ anti-bonding bands and resulting effects causes these predictions to be unreliable. For tubes with a diameter larger than 1 nm these small-scale effects are weak enough for the generalization to be viable. Measuring the inherent resistance of nanotubes require careful attention regarding the contact resistance. For short enough metallic CNTs, the conductance is shown to be that of a quantum wire, i.e. a wire that is so thin that electron movement in the transverse directions are quantized (Dresselhaus et. al. 2001:118) [1].

Due to the weak Van-der-Waals interaction between nestled nanotubes, the electrical properties of nanotube bundles are dominated by the axial conductance. This is covered in more detail in section 2.4

2.2.2 Mechanical Properties

As noted by Dresselhaus et. al, there are challenges when trying to define material characteristics to single CNTs (Dresselhaus et. al. 2001:289) [1]. Theoretical calculations are made using specific assumptions and approximations, while physical measurements suffers from practical issues. One example of research concerning the mechanics of CNTs is a study where an AFM tip was used to bend bundles of single-walled tubes over pores in a substrate (Salvetat J.-P. et. al. 1999). [8] The authors conclude that Young's Modulus of investigated slim and long CNT ropes were approximately 1 TPa, roughly five times that of steel. This is contrasted by the shear modulus of about 1 GPa compared to steel at 81 GPa (Nordling, Österman 2006) [9].

2.2.3 Thermal Properties

Thermal conductance in CNTs can be separated into two contributing factors, electrons and phonons. Depending on if a tube is metallic or semi-conducting, the electron contribution to thermal conductance takes different values (Yu et al. 2005) [10]. Regardless of which CNT type is investigated, there is an upper limit of heat spreading due to electrons. Since the thermal conductance varies with temperature, this results in a dominance of the lattice vibration contribution in the approximate temperature range of 110 to 300 K.

When the thermal conductivities of single CNTs with diameters of 1, 2, and 3 nm respectively were investigated, a group of researchers chose to measure the thermal conductance G (W/K) and chose a specific way to calculate the cross section area of the tubes. As noted above, there are sometimes no universally applicable characteristics of nanotubes, so assumptions has to be made. The functions of G were then, together with the implemented areas A and lengths L of the tubes, used to extract the thermal conductivity via the equation

$$\kappa = GL/A \quad (W/mK) \tag{2.1}$$

In the study referred to here (Yu et al. 2005) [10], the thermal conductivity between 100 and 300 K were calculated. The resulting graph showing the values for the different nanotube diameters is shown in Figure 2.5. A comparison of the thermal conductivity value at room temperature of the three tubes, as well as some common materials, is made in Table 2.1. As can be seen from this comparison, individual CNTs exhibit high thermal conductance, and show promise for use in heat spreading layers. For this project, the corresponding values for networks of CNTs are of more relevance, however. This is discussed in section 2.4.2.2

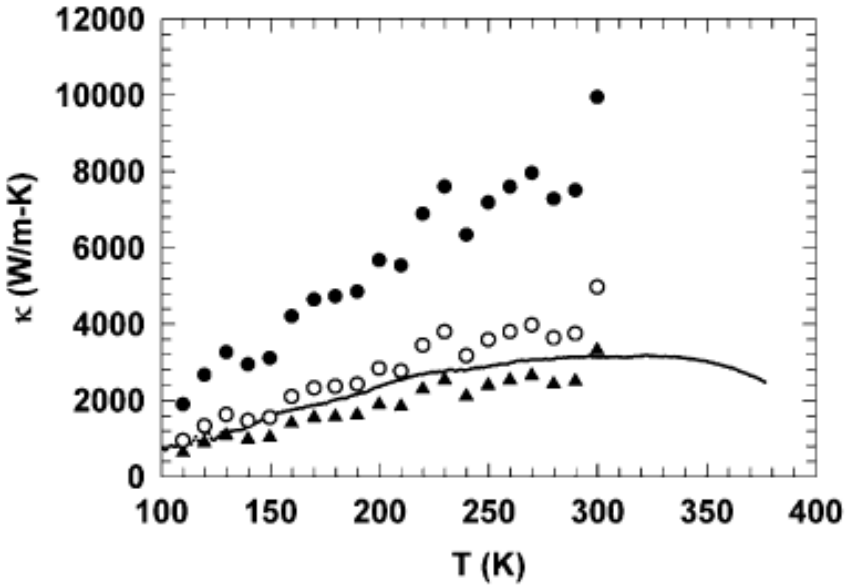


Figure 2.5: CNT thermal conductivity
Experimental measurements of on individual CNTs (Yu et al. 2005) [10].

Table 2.1: Comparison of thermal conductivity.
Thermal conductivity of individual CNTs and common bulk materials at room temperature (300K) (Nordling, Österman 2006) [9]. The values for the CNTs are linearly estimated from the measured data in 2.5 (Yu et al. 2005) [10].

Material (300 K)	Thermal Conductivity (W/(m*K))
CNT ($1nm$ diameter)	≈ 8700
CNT ($2nm$ diameter)	≈ 4400
CNT ($3nm$ diameter)	≈ 3100
Diamond	1000
Copper	400
Silver	418
Silicon	170
Aluminium	238
Gold	311

2.3 CNT Fabrication

The quality and configuration of CNTs, and thereby their physical characteristics, vary greatly depending on which fabrication techniques and post processing methods are used. A structured, illustrative categorization of common synthesis methods are shown in Figure 2.6, re-implemented from a review article concerning CNT fabrication (Prasek, J. et al. 2011) [11]. The machine used in this project, the Aixtron Black Magic 1 system, uses thermal chemical vapour deposition. This will be expanded upon in section 3.1.2.

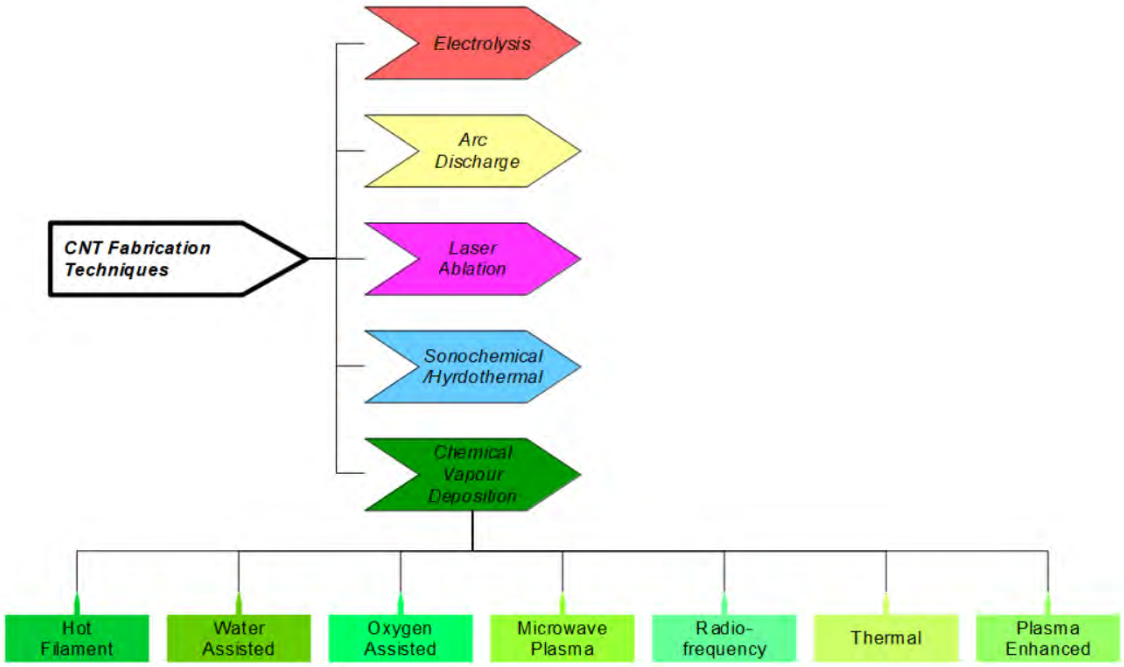


Figure 2.6: Graphic listing of different CNT fabrication methods.
Re-implemented from a CNT fabrication review article (Prasek, J. et al. 2011) [11].

2.4 Networks of Carbon Nanotubes

When ropes of CNTs, or individual specimens, are used in practical devices, they often form webs of interlocking strands, similar to the shape of spider webs. These networks have several interesting characteristics and phenomenons that are the result of different tube interactions.

2.4.1 Bonding Between Tubes

Using the differing characteristics of CNTs, interfaces with the standard metal-metal (MM), semiconductor-semiconductor (SS) and metal-semiconductor (MS) electronic structures can be realized using only nanotubes. The challenge lies in the electron transfer between differently structured tubes. For comparison, two different types of bonds between CNTs, covalent CNT bonds and wan-der-Waals intersections of

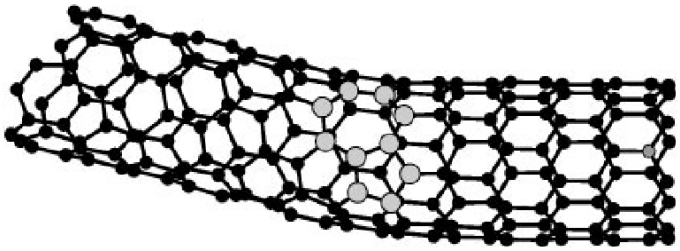


Figure 2.7: Seperate CNT tubes fused together (Postma, H. W. C. et al. 2000) [12].
Theoretical tube with a (8,0)/(7,1) junction. The gray dots indicate where atom hexagons have been replaced with a pentagon and a heptagon.

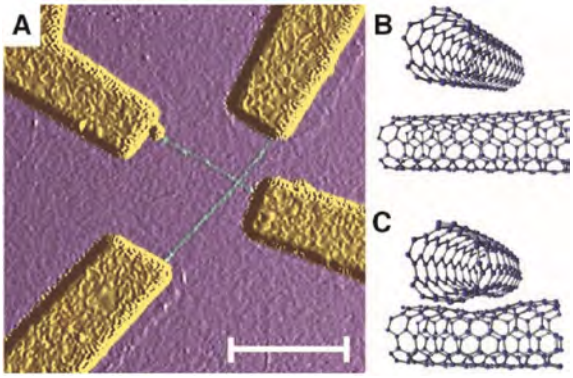


Figure 2.8: Crossing CNTs with VdW-interaction (Fuhrer MS et al. 2000) [13].
Van-deer-Waals bonding of two CNTs. (A) shows the experimental setup. (B) and (C) illustrates the difference between two free-floating tubes and the case where the top tube is pulled towards a substrate, deforming both structures.

CNTs, will be discussed here. They have both been studied by a research group using AFM and 2/4-probe measurements (Postma, H. W. C. et al. 2000) [12]. In this article, a basic comparison between the structures are made, using one buckled and two overlapping metal CNTs.

A buckled CNT is a simple example of, in essence, two nanotube structures covalently bonded end to end at a common interface. Both tubes have the same (m,n) value in this case, but other junctions between different (m,n) configured tubes with similar diameters could be formed. For instance, if two neighbouring carbon hexagon rings at the end of a (8,0) tube were to be replaced with a heptagon and a pentagon, it could form a covalent bond to one (7,1) tube. This is illustrated in Figure 2.7.

If two structurally intact CNTs are crossed and moved into contact with one another, no covalent bonds will be formed without external manipulation. Instead, standard van-der-Waals interaction will attract the tubes to each other at the crossing point. Electrons can still be transported from one tube to the other by tunneling through the potential gap at the intersection, making conduction through the structure possible. As can be seen in figure 2.8, tubes crossing on a substrate will be deformed due to the van-der-Waals attraction between the top tube and the substrate. Calculations have shown that the decrease in distance and the deformation significantly increased the tunneling probability due to the overlap of the electron wave functions of the two tubes (Fuhrer MS et al. 2000) [13].

A more complex structure consisting of a multitude of separate strands or bundles of CNTs that have electric contact with each other are often referred to as CNT meshes. Such networks of tubes can, if they cover a large enough area, be compared to thin films of other electrically conductive materials.

2.4.2 Basic CNT Network Thin Films

Following early production examples of thin-film CNT networks (Chen et al. 2003) [14], researchers have developed schemes with the goal of integrating such networks into micro scale devices. Several areas of interest have unfolded where these networks might replace other, more traditional materials.

2.4.2.1 Electrical and Optical Properties

As discussed in chapter 1.1.2, the inherent electrical properties of CNTs makes them a potential replacement for standard materials such as Indium-Tin Oxide (ITO) in electric structures. If made sufficiently thin, such CNT thin films do also have comparable transparency to ITO, further suggesting it as a viable alternative.

One early study of a CNT thin film, as a 1 kÅ thick transparent electrode in a quantum-well light-emitting diode structure (Lee et al. 2004) [15], indicated a contact resistance one third of the standard contact materials (specifically Ni/Au in this case). Here, the nanotubes where dissolved and applied en masse, forming a 1000 Å thick web of van-der-Waals bonded strands where the resistivity was measured to be around $1.5 \times 10^{-4} \Omega cm$. This corresponds to a sheet resistance of $15\Omega\square$.

Thicker films are of course more conductive than thin films. However, it is only thin networks of CNTs that are highly transparent, due to the high absorbance of graphene-based materials. In one study, researchers examined thin films of CNTs as hole collector electrodes in organic solar cells (Pasquier, A. D. et al. 2005) [16]. In their experiments, a 20 nm thick thin film had approximately 80 % transparency for photons of 325 nm wavelengths. The corresponding value for a 200 nm thin film was around 20 %.

The qualities of van-der-Waal bonded CNT networks examined in the studies mentioned above seems to indicate them as viable structural components. This may be true, but in many cases where simultaneous transparency and conductivity is critical, these alternative thin films are not reasonable alternatives for standard materials such as ITO, as discussed in section 1.1.2.

2.4.2.2 Mechanical and Thermal Properties

One potential use of CNT networks is as part of a composite material where strength is important. In a study concerning flexible electronics (Jia, L.-C. et al. 2017) [17], CNTs was dissolved along with natural rubber and pressed into a flat hybrid material. This compound has been designed as a bendable, stretchable and twistable

shield layer for electromagnetic interference in microelectronic applications. Two characteristics that were investigated, namely strain limit and mechanical degradation, compared favourably to other electronic devices. Also, the Young's modulus of the material was measured and was found to be about 7.3 MPa at 10% CNT weight percentage, which is an increase of MPa by 943% compare to ordinary rubber. Using CNTs as a strengthening material, like iron bars in reinforced concrete, seem to be a viable technique for applications with similar requirements.

Another feature of CNT networks are their ability to transfer heat. When talking about thermal conductivity of multi-walled CNTs or ropes of single-walled CNTs, there are two directions of thermal conductance, along the tube axis (on-tube) and between nanotube surfaces (inter-tube) (Dresselhaus et. al. 2001:277) [1]. For networks of CNTs, the importance of inter-tube phonon dispersion for thermal conductivity only increases.

In this project, a method for using CNTs in combination with Ni-particles as a thermal spreading layer is suggested. Such layers vary greatly in effectiveness depending on fabrication methods, as well as substrate material and temperature when measurements are made (Duzynska, A. et al. 2015) [18]. If a thin film is fabricated using the technique suggested in this thesis, great care will have to be taken when characterizing the layer in order to obtain a fair comparison to alternative methods.

2.4.3 Improved Characteristics

2.4.3.1 Chemically Bonded CNTs

One of the ways the electric and heat conductivity of CNT meshes, along with stress resistance, could improve is to implement actual covalent bonds between tubes. One method to accomplish a form of intertube connections have been proposed in a study where electron irradiation was used to change the atom structures in localized areas of CNT bundles (Kis, A. et al. 2004) [19]. A theoretical model based on density functional theory indicated possible atom configurations between CNT-ropes. The results obtained from mechanical bending of CNT-ropes was that the bending modulus for bundles treated in this manner increased up to 30-fold compared to that of the original nanotube ropes for short irradiation times. For longer irradiation doses, the structures became amorphous, thus counteracting the stabilization of the bridges.

2.4.3.2 Doped CNT Networks

Instead of implementing bonds between CNTs, aspects of a mesh may be increased by improving the properties of the individual tubes. One way of doing this is to replace carbon with other atoms in the CNT lattice. Dopant atoms affect the energy band structures of the material, and thus the behaviour of electrons in the networks. By choosing different dopants and tuning the fraction of replaced carbon atoms, selective properties might be augmented to a level suitable for a potential practical use.

By using boron as a dopant, researchers have studied the possibility of fabricating a network of superconducting CNTs (Haruyama, J. et al. 2011) [20]. In their study, the measurements made on the fabricated B-SWNT thin film indicated it as being a type-II superconductor. Such materials exhibits a hybrid state of normal and superconductive behaviour in certain conditions between a standard and superconducting phase. Even though an optimal dopant atomic percentage were not found in the study, superconductive tendencies were strongest at low percentage values of boron, roughly 1.5 %. Further optimization of the doping level might lead to even more efficient conductivity, according to the researchers.

2.4.3.3 Particle Bridges as an Alternative

The idea behind the current project is to enhance the thermal conductivity between CNT strands by using nanoparticles as bridges between them. Ni-particles are used in this manner due to the interplay between Ni-surfaces and carbon molecules (Lahiri, J. et al. 2011) [21]. The researchers have studied graphene that was grown using ethylene on a Ni-surface, causing the carbon atoms to spread over the area. It can visually be described as CNTs melting down over the Ni. One of the two main objectives of this project is to investigate if this effect can be achieved at the interface between the Ni-particles and CNTs in the fabricated networks.

2.5 The Ineffectiveness of Tunneling

Standard CNT meshes will, as mentioned in the previous section, not have chemical bonds between tubes. This means that the electrons transfer between tubes at junctions due to tunneling effects. This results in an in-built resistance that lowers important characteristics of the network, such as electric conductance.

In order to demonstrate the effect of tunneling junctions in CNT networks, a simulation have been performed using Matlab. A single CNT-CNT junction is considered, as is illustrated in Figure 3.5. To obtain an average tunneling reistance value, a large number of electrons are simulated passing through the junction. In Section 3.4, the calculations are summarized and explained visually. The code used in Matlab can be seen in Appendix 1.

3
Methods

3.1 Carbon Nanotube Growth

As noted previously, there are several methods that are commonly used when preparing carbon nanotubes of varying dimensions and number of walls. The method available for this project was growth by chemical vapour deposition. This method also allowed for a reasonable control over the diameter and length of the tubes.

3.1.1 Substrate Preparation

To obtain the substrates used for carbon nanotube growth, a cleaned silicon wafer 3 inch in diameter was mounted in an AVAC evaporation system. At a rate of 1 Å/s the wafer was coated with a 10 nm layer of AlO_3 catalyst support and a 1 nm Fe catalyst layer.

To protect the deposited layers when cutting them into the desired substrate size, a thick layer of S1813 photoresist were applied on top of the wafer. This was done with spin coating at 3000 rpm for 45 s, after which the substrate was baked at 130 °C for 45 s. When this layer had been applied, a diamond saw dicing machine of the brand Loadpoint Microace 3+ was used to cut the wafer into 1x1 cm substrates.

3.1.2 Chemical Vapour Deposition

With the substrates diced, they where submerged in acetone and cleaned using an ultrasonic bath at a high frequency for 10 minutes. When the resist had been removed, they where placed into the carbon nanotube growth system Aixtron Black Magic 1, seen in figure 3.1. The system is operated through the use of programmed recipes. The flowchart of a specific recipe is shown in Appendix 2. Importantly, the pre-heating of the substrates was performed at 495 °C for 180 s. The growth occurred at 720 °C for 35 and 175 s respectively using C_2H_2 as precursor.

3.2 Formation of Nanotube Network

In order to obtain a Ni/CNT network, solutions of nickel-oxide particles (NiO_x) were mixed with solutions of nanotubes. The resulting mixtures was then applied to substrates and dried to form a thin layer of hybrid material.



Figure 3.1: Aixtron Black Magic 1. This is a self regulated CVD system intended for CNT growth.

3.2.1 Solution Preparation

A small amount of NiO_X nanoparticles was dissolved in acetone to form a mother solution from which later solution was made. Exact concentration of particles where not of practical importance, since the quality of any end result film would be examined based on obtained characterization results. Before withdrawing any of the solution for use, the vials were placed in an ultrasonic bath at a high frequency for 10 min.

The CNT solutions used was obtained in a similar way. Substrates covered in CNTs of different lengths was placed in vials of acetone and placed in an ultrasonic bath at high frequency for 10 min. This released the CNTs from the substrate surface and spread them through the acetone, after which a rough amount of solution volume was extracted. After combining the two different solutions into one vial and performing yet another ultrasonic mixing, a volume of the mixture was applied to a clean Si substrate and left to dry. When sufficiently dried out, the samples were examined in order to determine the quality of the Ni/CNT network.

Based on observation of earlier substrates, the mother solution and the various generations of offspring solutions was used in combination with CNTs of approximately equally scaled concentrations to form unique thin films. Different CNT lengths, applications techniques and concentration proportions were visually investigated in an iterative process to find a suitable fabrication method in which the obtained network possessed the desired configurations. These observations, and comments regarding the differences between them, have been tabulated in chapter 4, Results.

An important note is that at a later stage, a new mother Ni-solution had to be created. To obtain approximately the same concentration of Ni-particles in the acetone

Table 3.1: Thermal treatment of substrates.
The different annealing times of the five substrates that were thermally treated.

Substrate	Annealing time (900 K)
A	-
B	2 min
C	4 min
D	8 min
E	20 min

solvent, a basic amount was guessed as a first step. Then, a known concentration of CNT solution was used to form networks with the new Ni-mother that were compared with the corresponding old Ni-mother substrates. Based on this visual inspection, more acetone was added to the new Ni-mother to compensate. After one further iteration of the same inspection, the new Ni-mother solution was deemed to be acceptably close to the first Ni-mother that the main project process could continue.

3.2.2 Deposition

3.2.2.1 Drop Coating

The primary means of applying the Ni/CNT solutions onto the substrates was through drop coating. A small amount of the mixed liquid was extracted with a pipette and slowly emptied onto the silicon square. When doing this, the hybrid material formed in small clusters on the surface, with empty, or sometimes Ni-covered, areas between them. On the final substrates, three steps of drop coating was performed. When this was done, the vial with the fluid was ultrasonically mixed for 30 min, with each application 10 min apart.

3.2.2.2 Spin Coating

For comparison, the same amount of solution that were drop coated onto the substrates were spin-coated on a separate set of samples. The spin-coating was performed at 6000 rad/s for 8 s, with an acceleration of 3000 rad/s^2. The solution concentration used was that of the optimized substrates. No spin-coating was done for the longer CNTs.

3.2.3 Annealing

When a suitable network fabrication process had been determined, five substrates was produced in order to investigate the effects of thermal treatment on the networks. For this step, the heating plate of the Black Magic system was used. One sample was left untreated as a reference. The other substrates was subjected to the same heating program with different time spans at the maximum temperature. The processes are summarized in Table 3.1. The recipe used is detailed in Appendix 3.

3.3 Characterization Techniques

3.3.1 Scanning Electron Microscopy

When investigating structures on a small scale, there are many methods to make use of depending on what information is needed. In this project, the structure of produced Ni/CNT networks have been visually investigated using Scanning Electron Microscopy (SEM).

SEM is a form of electron microscopy, where electron beams are used in contrast to optical microscopy that relies on photons. The possible wavelengths of an electron microscope are on a different scale than that of visible light, with resolutions of a whole different order possible. In electron microscopy, the use of magnetic fields is analogous to the use of lenses in optical microscopy. The surface is scanned in a raster pattern, producing graphical images that can be examined. The SEM setup used in this project is shown in figure 3.2.



Figure 3.2: SEM installation. This is the SEM system used for investigating the Ni/CNT networks.

When making an SEM scan of a surface, an electron source accelerates the particles to a desired kinetic energy with a corresponding wavelength. The electron beam emitted is focused by one or more magnetic lenses and directed towards the sample, which must be small and resistant enough to be placed on the microscope stage in vacuum conditions. When interacting with the sample, electrons are reflected back towards the source where detectors have been placed. The intensity of back scattered electrons depend on the mass of the atoms at the surface, making back scattering useful for investigating the material composition of different areas.

There are also inelastic scattering of the source electrons, resulting in secondary electrons being generated. These are electrically attracted to a collector which measures the intensity of this secondary electron stream. Depending on the angle of impedance of the primary beam, varying amounts of secondary electrons are able to

be captured by the electric attraction. This difference in surface topography is used to generate an image where surfaces orthogonal to the primary beam are darker than more tilted areas. The result is a graphical image that depend on the surface topology.

Further examining of the sample can be done by measuring the electromagnetic radiation emitted during the process. This occurs when outer shell emits photons and occupies orbits closer to the nuclei, which has been emptied due to inelastic scattering. Using this method, it is possible to investigate the relative concentrations of atom numbers in the sample. Another possible investigative method is to measure the current absorbed by the sample at the raster points. This results in a map over the current distribution of the surface.

In this project the information of interest is the topological nature of the produced substrates. The detection of secondary electrons have therefore been used to obtain visual representations of the Ni/CNT networks.

3.3.2 Raman Spectroscopy

To investigate the effect of thermal treatment on the chemical structure of the networks, Raman spectroscopy was performed. This method uses laser light to detect varying forms of excitable quantum states present in materials. This is a common way of studying the lattice properties of graphene and CNTs, where it amongst other things can be used to estimate the disorder of the atoms and identify the most abundant tube diameter present on the substrate.

In standard Raman spectroscopy, a laser or monochromatic light source is directed towards the substrate, where the photons are subjected to inelastic scattering. The shift in photon energy that is recorded after the interaction with the substrate depends on which quantum system it excited, be it lattice or atom pair vibrations, or indeed rotational phases of chemical bonds. It is therefore possible to deduce certain atomic configuration aspects of the investigated material from the obtain Raman shift spectra.

In Figure 3.3, typical Raman spectra of various carbon structures are shown (Dresselhaus, M. S. et al. 2010) [22]. Important peaks corresponding to different quantum systems are denoted. The G and G' peaks arise from interaction with sp^2 materials, and are therefore common to all of the illustrated spectra. The peak marked as RBM is so called because of its relation to the frequency of the CNT circumference deformation. As for the D and D' peaks, these correlate with disorder or irregularities in the basic hexagonal graphene lattice. As a comparison, the D peak of CNTs, which can be thought of as rolled up graphene, is much smaller than for outright damaged graphene. However, for pristine graphene the D peak is barely registered, if at all.

All of these observations makes Raman spectroscopy a powerful tool for finding the

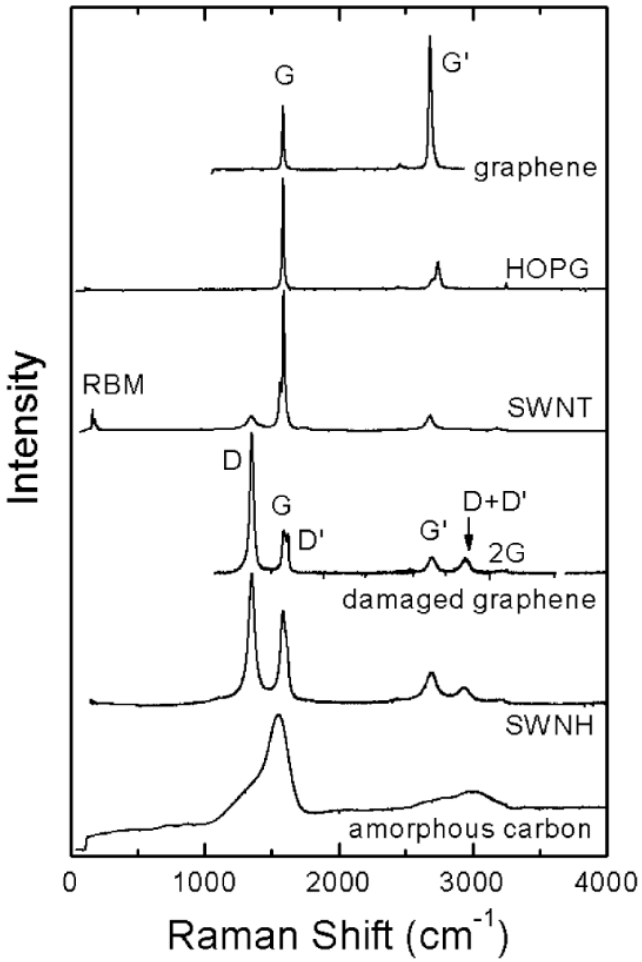


Figure 3.3: Raman shift spectra of carbon structures
Typical Raman shift plots with annotations for various different carbon atom molecules [22].

fingerprints of molecular carbon samples. In this project, the intensities of the G and D peaks are of fundamental interest, along with the corresponding G' and D' peaks. Shift in peak height or position might give hints towards the reaction of the Ni/CNT interfaces to annealing.

For this project, a WITec alpha300 R Raman microscope was used. The installation can be seen in Figure 3.4.

3.4 Simulating a CNT-CNT Tunneling Junction

To perform a simulation that illustrates tunneling resistance in a reasonable time span, certain abstractions and simplifications have been made. Important values that are easily looked up have been used, while others have been assumed for simulation convenience. The set up values of the calculations can be seen below in Table 3.2.

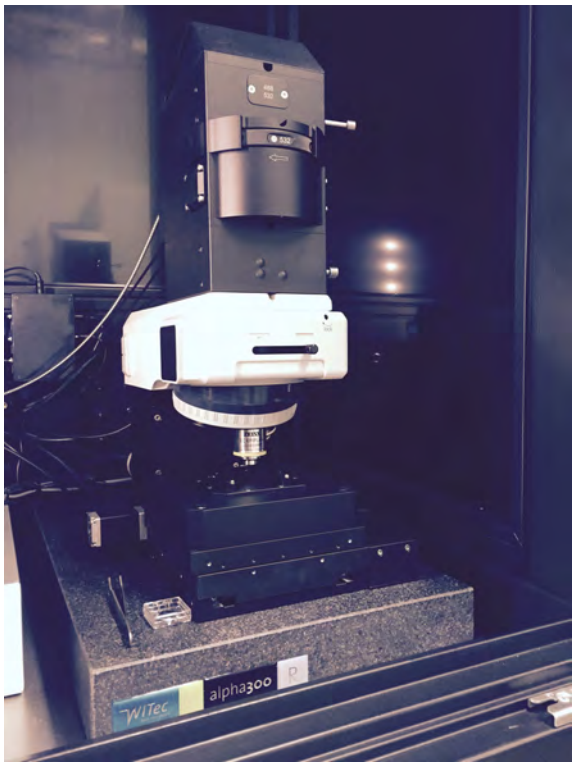
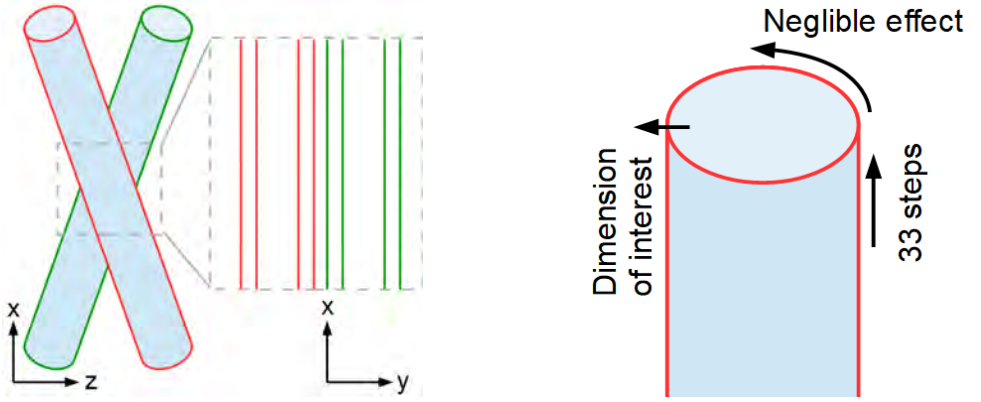


Figure 3.4: WITec alpha300 R
This is the Raman installation used for the project. The locations of the scanning points, as can be seen on optical images of the substrates, are displayed in Appendix 4.



(a) Two diferent views of a CNT-CNT junction.

(b) Assumptions regarding 1D tunneling calculations.

Figure 3.5: Geometry of the simulated CNT-CNT junction.
Only one electron wave dimension is considered when calculating the tunneling probability. The electron wave packet that would move along the length of the tubes is abstracted by using 33 distinct steps along the junction. The quntized part of the 3D wave function along the perimeter of the tube is ignored for the purpouse of inter-tube tunneling. The only quantization considered is therefore in the radial direction, between the CNT walls of the first and second tube.

Table 3.2: Simulation input values.
These are the parameters that were used to simulate a CNT-CNT tunneling junction.

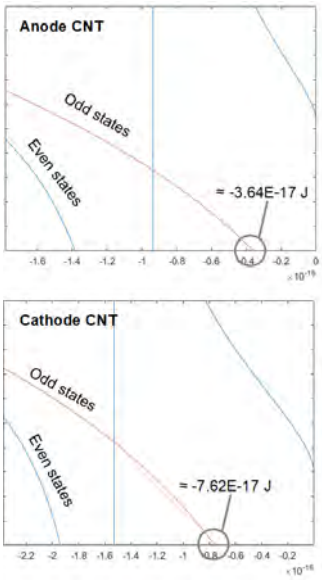
Physical characteristics	Assumed values	Calculation abstractions
electron mass $m_e = 9.12 * 10^{-31}$ kg	potential well depth 1300 eV	discrete electron transport *33 steps along junction*
Planck's constant $\hbar = 6.63 * 10^{-34}$ J/Hz	applied voltage 370 eV	simplified tunneling calculations *only 1D tunneling considered*
Graphite layer distance $d_{Gr} = 0.335$ nm	Quantum well width $d_{Gr}/2$	interpolated probabilities *Only 4 probabilities calculated*

The intent of the calculations is that the applied voltage will cause a simulated electron to move along one CNT wall towards the minimum junction distance. At a certain point, the electron will tunnel over to the neighbouring CNT wall and exit the junction on the other side. Each calculation step required to set up this simulation is listed below.

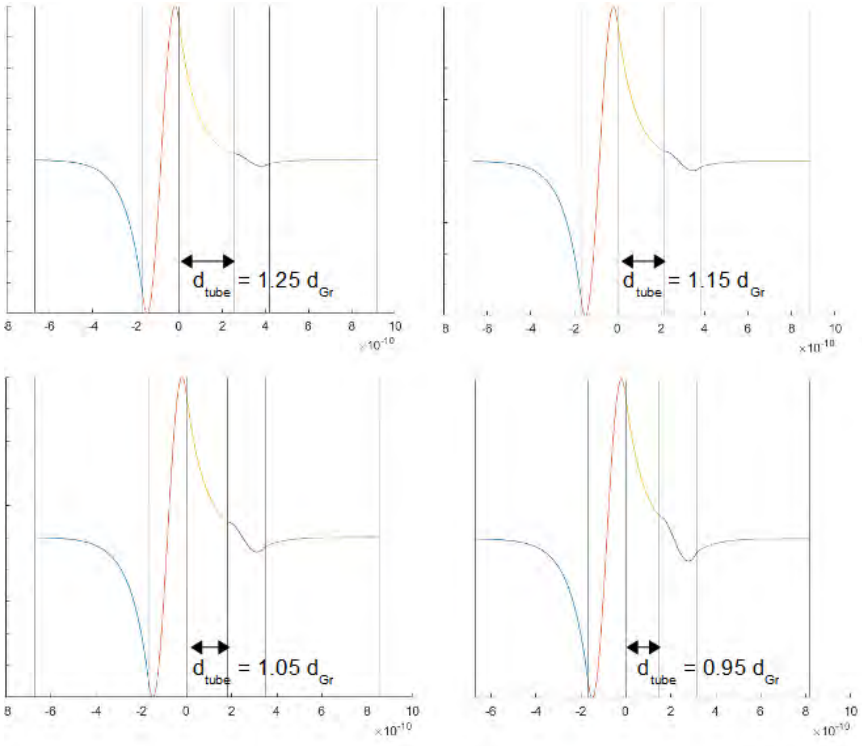
1. Find the probability functions of predetermined positions.
    - Calculate approximate quantum energy levels.
    - Find the wave functions at four CNT-CNT distances.
    - Calculate the normalized probability functions.
2. Construct a tunneling probability map across the junction.
    - Determine the probability of tunneling at the predetermined junction positions.
    - Interpolate the tunneling probability along the junction for all 33 position coordinates.
3. Set initial conditions and define process parameters.
    - Set the starting position for the incoming electron.
    - At each position, randomize if the electron tunnels or not. Then move the electron one position closer to the anode.
    - Collect all step positions in a matrix.

3.4.1 Probability Functions

Square potential wells were assumed for these calculations. The depth of the energy wells and the applied voltage were chosen in a manner as to facilitate the calculation. When these values were used, the two lowest quantized electron wave energy levels were found for both the anode and the cathode side tube. The graphs generated can be seen below in Figure 3.6a. Also for calculation convenience, the second lowest energy level was used for both sides of the junction. The corresponding anti-symmetric wave functions were found at four different wall-to-wall distances, for both tubes. The wave functions for electrons located in the tube connected to the cathode are shown in Figure 3.6b.



(a) Quantized energy levels.



(b) Corresponding wave functions at four different tunneling distances.

Figure 3.6: Energy levels of the tunneling electrons.
The lowest odd energy levels were assumed for both CNT tube electrons, for ease of calculation. For each side, the tunneling wave function is calculated at four different tunneling lengths. Note that a small compression of the tubes is assumed at the closest gap, as can happen due to van der waal-forces between the topmost tube and the substrate.

Squaring and normalizing the wave functions allows for the calculation of the tunneling probability at the four predetermined distances. In Figure 3.7, the probability functions of the CNT connected to the cathode are shown. The tunneling probability is obtained by comparing the amplitude of the wave functions in the two quantum wells, meaning that $Prob_{tunn} = A_{CNT2}/A_{CNT1}$.

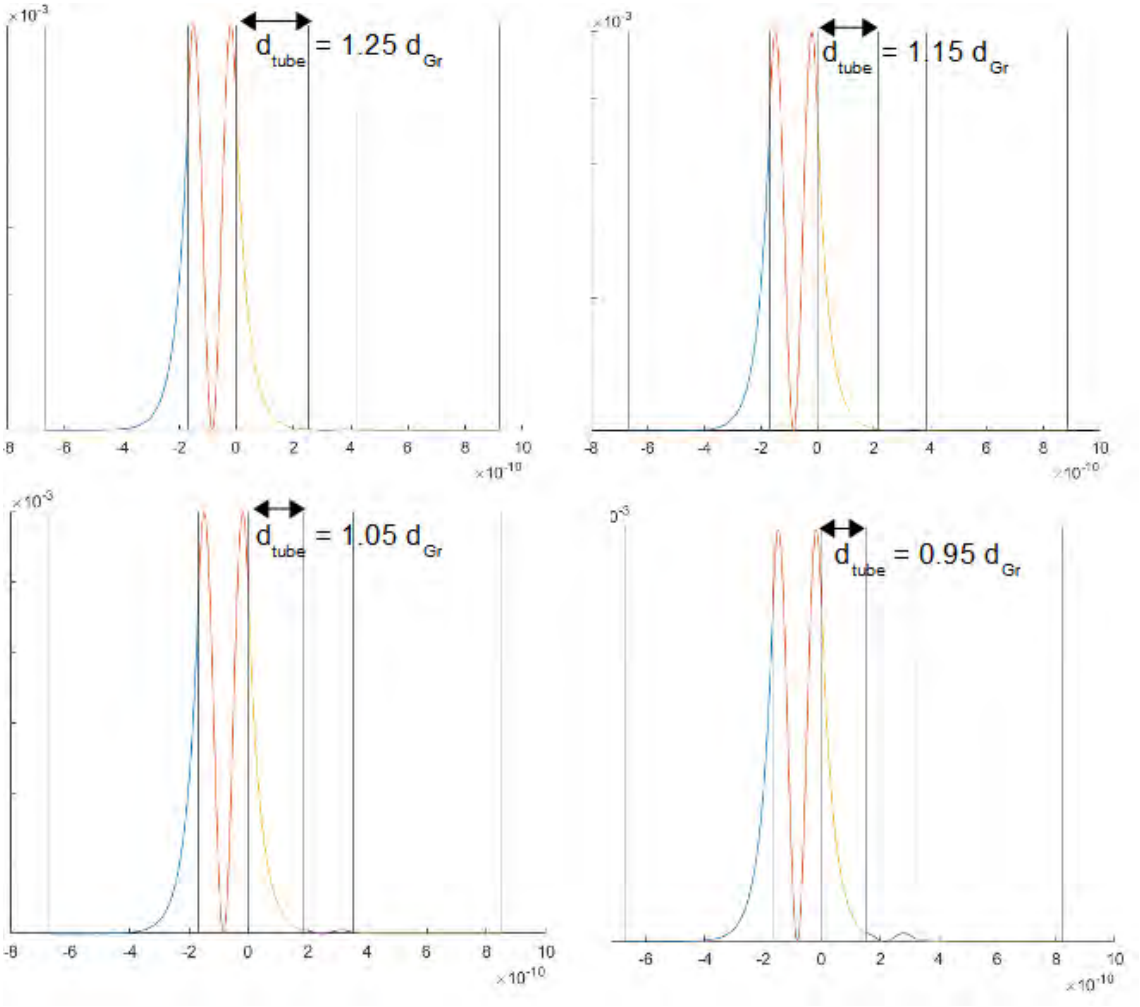
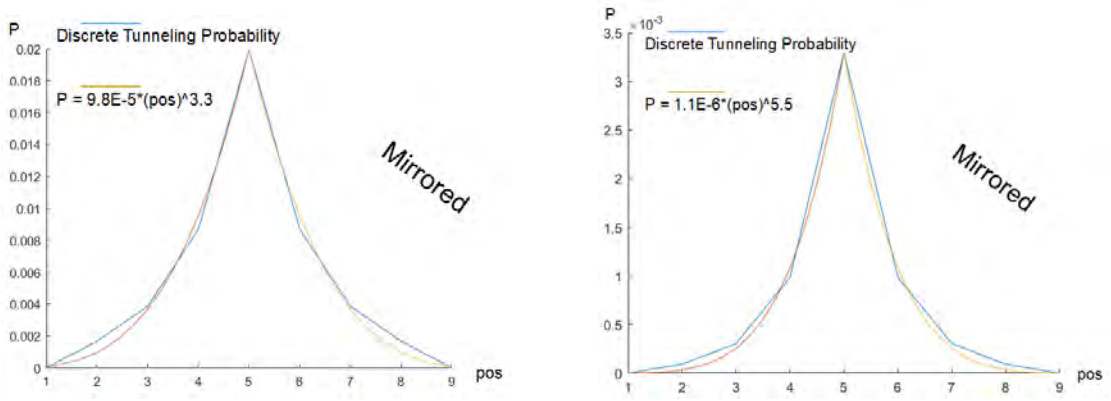


Figure 3.7: Probability functions for the junction.
The amplitudes of the probability function on each side of the barrier determines the probability of tunneling. Note that these functions correspond to electron waves in the cathode connected tube.

3.4.2 Tunneling Probability

To obtain a reasonable approximation of tunneling probabilities between the predetermined barrier widths, an interpolation was made for both tubes. The interpolation functions are compared to the actual values calculated in Figure 3.8. As the tunneling probability of the widest barrier, $1.25 * dGr$, is close to 0, the probability of tunneling for greater distances than that is assumed to be negligible.



(a) **(b)**

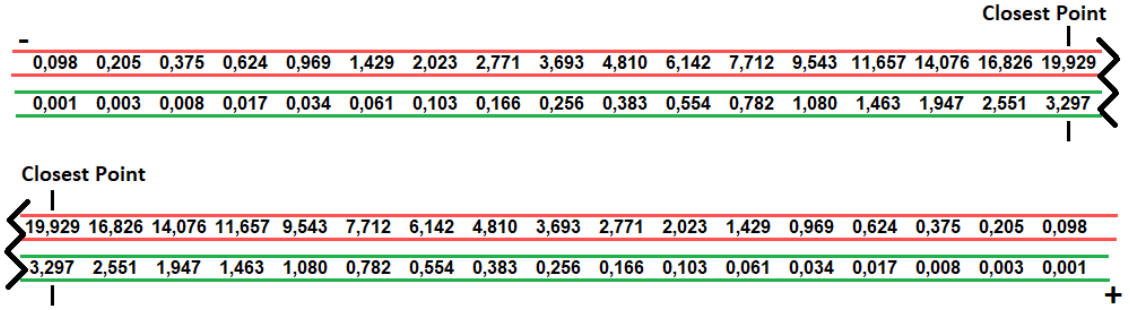
Figure 3.8: Interpolated tunneling probability.
In order to simplify the simulation, only 4 different tunneling probabilities were calculated. The probabilities of tunneling in the range of these barrier widths were interpolated. (a) is the interpolation of the cathode connected CNT. (b) is for the anode connected CNT.

3.4.3 Conditions and parameters

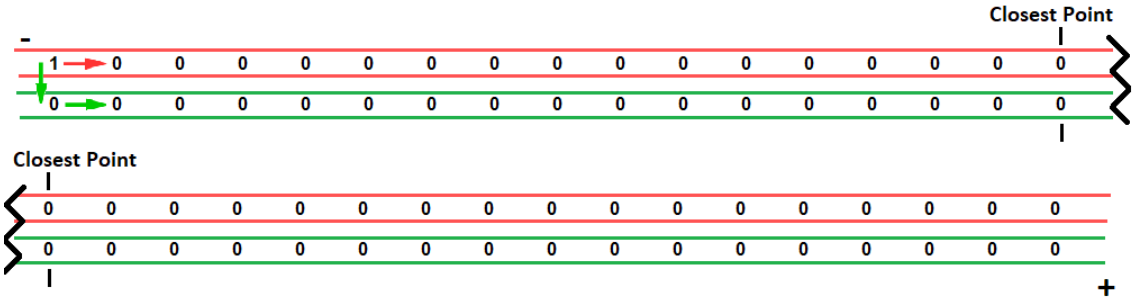
A total of 33 tunneling probabilities have thus been generated for both CNTs, one for each possible electron position in the simulation. They are listed in figure 3.9a. The simulation works by randomizing a tunneling event for an electron at the corresponding position. Regardless if the tunneling occurs or not, the electron is then moved towards the anode end of the junction. This means that for the first CNT, the electron moves towards the closest point position, while it always moves towards the far end while in the second tube. A visual description of this is shown in Figure 3.9b. Once the electron have reached the position on the far side of the junction, another iteration of the simulation is started.

A total of 100 simulations were performed using the above method. Each instance was terminated when the electron reached the final position, or when 200 iterations were reached. For each simulation, the number of iterations were recorded. This value was used to calculate the increase in resistance across the junction as compared to non-hindered CNT electron transport.

In addition, all position matrices of every simulation were added together in order to obtain a visual representation of an average junction crossing. The compounded position matrix was used to generate the probability of finding the electron at a certain junction point at a random time. Together with interpolated probability functions for all electron positions, this allowed for weighted probability functions at every step along the junction.



(a)



(b)

Figure 3.9: Probability and position matrices.
(a) shows all probabilities of tunneling for each possible electron position in the junction. (b) shows the initial electron position in the simulation. Also, the two different paths that the electron could potentially take before the next time step are here illustrated with arrows.

4

Results

4.1 Carbon Nanotube Array

Two of the substrates grown in the Black Magic CVD system are shown in figure 4.1. Four samples, two with a shorter growth time of 35 s and two with a longer growth time of 175 s, was produced. The recipe of the Aixtron Black magic 1 growth program is displayed in Appendix 2. One specimen of each CNT length was dissolved for use in the fabrication process. The other two were investigated by SEM imaging, as can be seen in Figure 4.2. They were inserted in the SEM chamber on a holder at an angle of 45° and measured using the software of the setup.

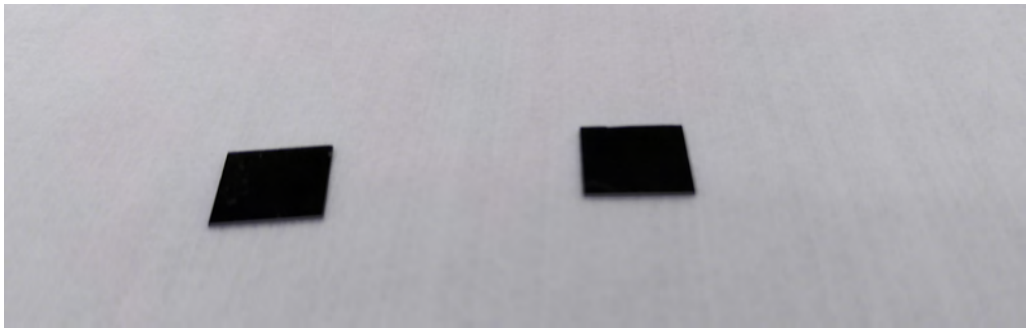
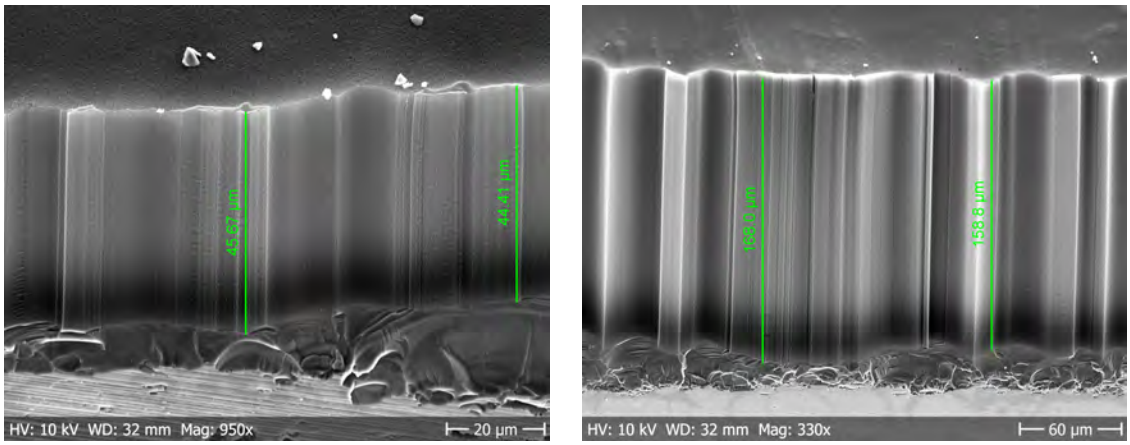


Figure 4.1: Substrates with CVD-grown CNTs.
The left substrates have the sorter carbon nanotubes. The longer nanotubes are on the right substrate.

The nanotubes were measured on multiple locations on both substrates and an approximate average height value were determined. A couple of representative measurements per sample are shown in Figure 4.2, where the projected nanotube lengths were close to the approximate heights of 45 μm and 164 μm respectively. The actual lengths were calculated using the standard trigonometric equation 4.1 spelled out below. The shorter nanotubes were calculated to be approximately 64 μm long. The longer nanotubes were found to be 232 μm in length.

$$L_{actual} = L_{measured}/cos(\pi/4) \tag{4.1}$$

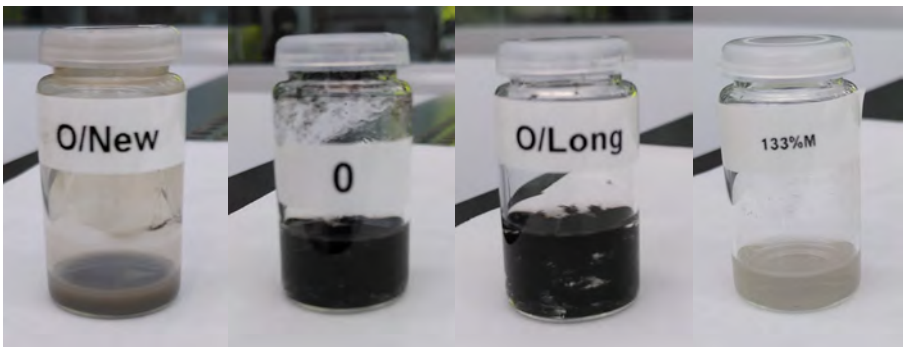


(a) **(b)**

Figure 4.2: Grown CNTs of different lengths
Images of grown CNTs at 45° inclination. (a) The CNTs grown for 35 s. (b) The CNTs grown for 175 s.

4.2 Ni and CNT Solution

The vials containing the two CNT solutions, one with short and one with long CNTs, and the second baseline Ni-particle solution are shown in the images of Figure 4.3.



(a) **(b)** **(c)** **(d)**

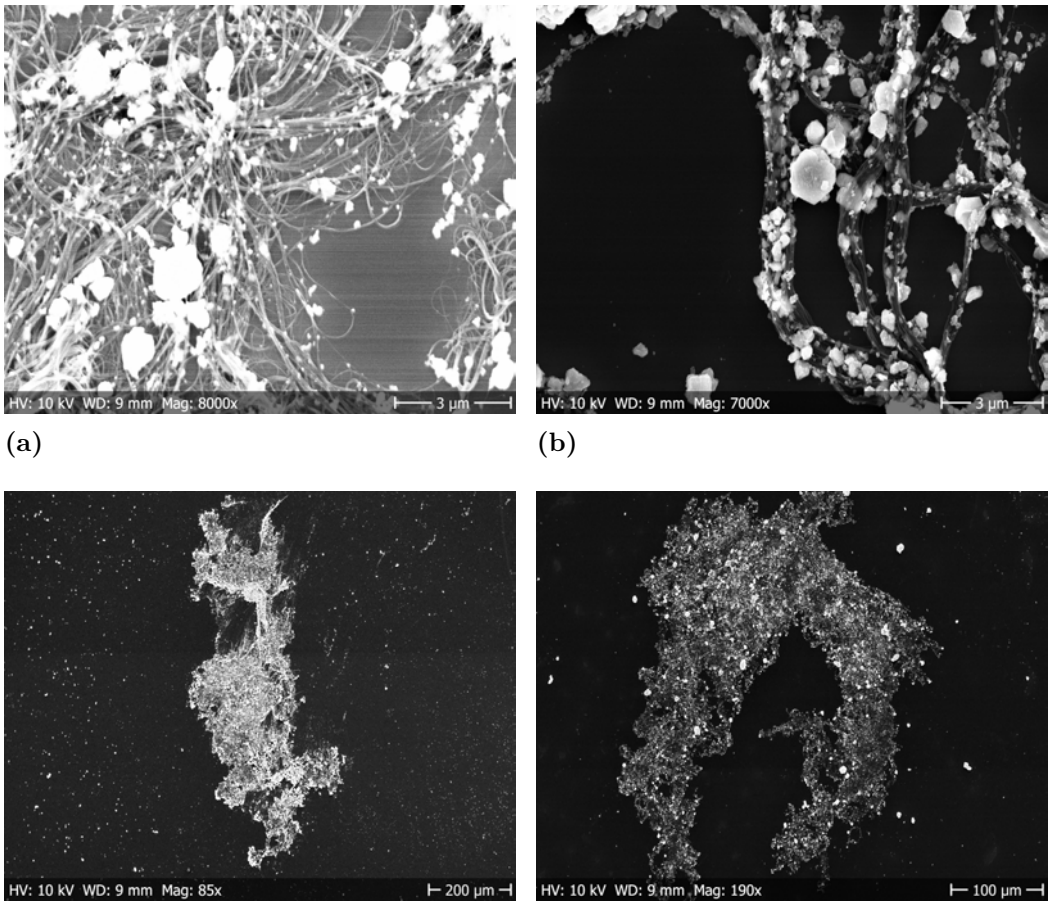
Figure 4.3: Baseline Solutions.
Newly shaken vials. From left to riht: Ni-particles, 64 μm nanotubes, 232 μm nanotubes and the solution mix used for the final networks.

4.3 Networks

4.3.1 Iterative Optimization

Varying aspects of the fabrication process yielded different structures of the drop-coated networks. The primary way of investigating the networks was with SEM imaging. The images in Figure 4.4 shows the difference between reference networks

and other meshes that were fabricated with one aspect changed. The effects of longer tubes and an alternate application method could be evaluated. The way forward was deemed to be drop coating with the Short CNT/Ni solution.



(a) **(b)**

(c) **(d)**

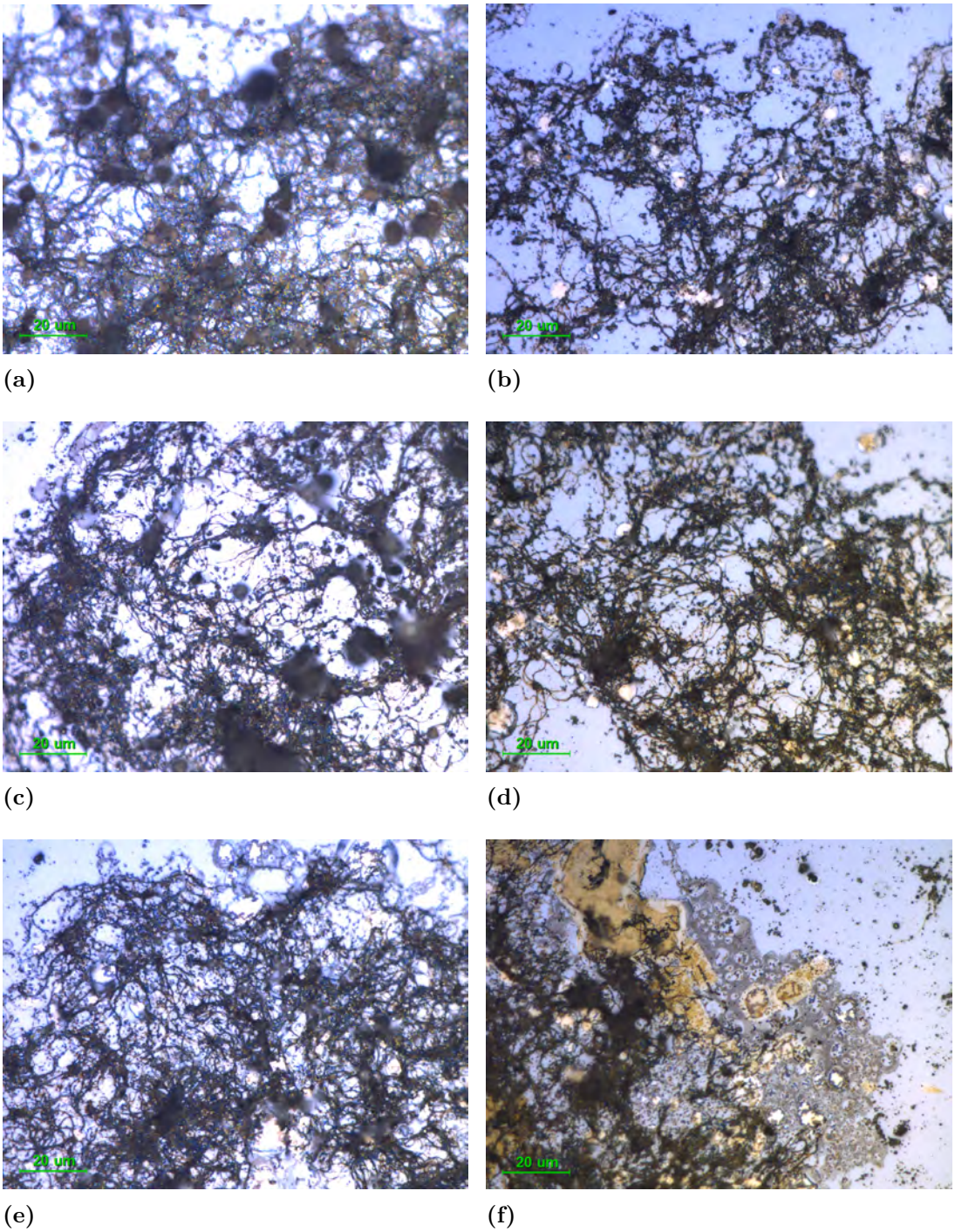
Figure 4.4: Comparison with alternatives
During the iterative optimization process, longer tubes and spin coating was tested for viability in generating networks. In the top row, an SEM image of a short tube network (a) is compared to a long tube mesh (b). Longer tubes was deemed to result in clumpier webs. Image (c) is of a typical drop coated Ni/CNT mesh that, next to a spin coated mesh in (d) appears to be roughly two times bigger. Drop coating was therefore kept as the application method from then on.

4.3.2 Thermally Treated Optimized Networks

When an acceptable standard of network quality was met, five samples were produced in the determined fashion. The same concentration of Ni/CNT/Acetone was deposited using the three-step drop coating method. The Networks were then annealed using the Black Magic CVD setup. The resulting networks have been studied optically as well as through SEM imaging and RAMAN spectroscopy.

4.3.2.1 Optical Investigation

In Figure 4.5, local microscope images are shown of the substrates.



(a) **(b)** **(c)** **(d)** **(e)** **(f)**

Figure 4.5: Optical images of annealed samples.
The different annealing times for the samples in the images are (a) no annealing, (b) 2 min, (c) 4 min, (d) 8 min and (e) 20 min. In image (f), unexpected formations below the nanotubes were found. The yellow areas have surprisingly straight edges at many locations. This can be seen more clearly in the corresponding SEM images.

4.3.2.2 SEM Investigation

The following images in Figure 4.6 are the SEM images of the same substrates that were presented in Figure 4.5.

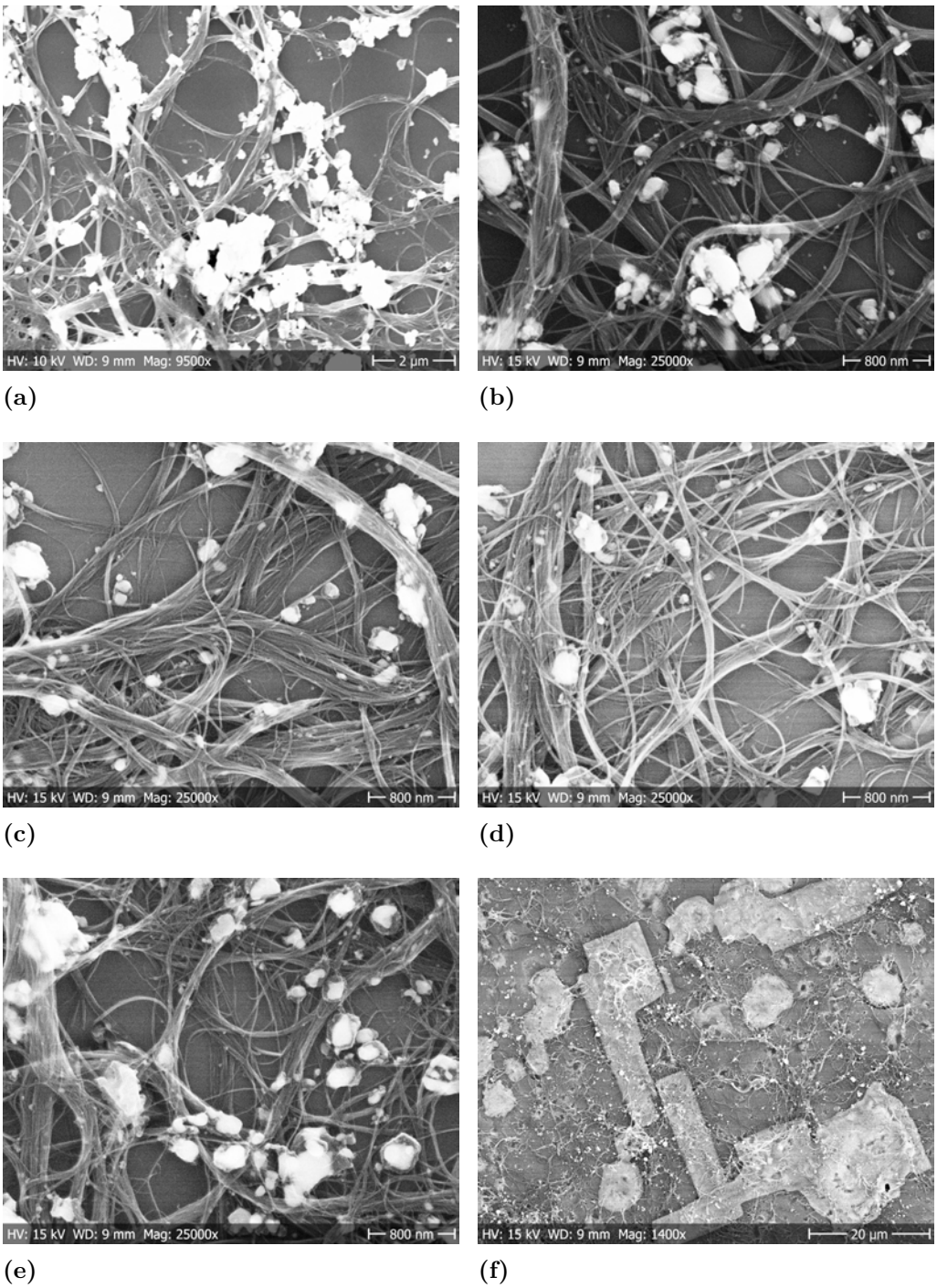


Figure 4.6: SEM images of annealed samples.
The different annealing times for the samples in the images are (a) no annealing, (b) 2 min, (c) 4 min, (d) 8 min and (e) 20 min. In image (f), the unexpected formations below the nanotubes are clearly shown to have straight lines at large part of the formation edges.

4.3.2.3 Raman Spectroscopy

For each substrate, Raman spectroscopy was performed at a total of ten points, with two groups of five points from separate areas of the network. In Figure 4.7, the average intensity of the Raman shift specta are plotted for each substrate. The corresponding optical images are presented in Appendix 4. The Matlab code used to plot the graphs is laid out in Appendix 5.

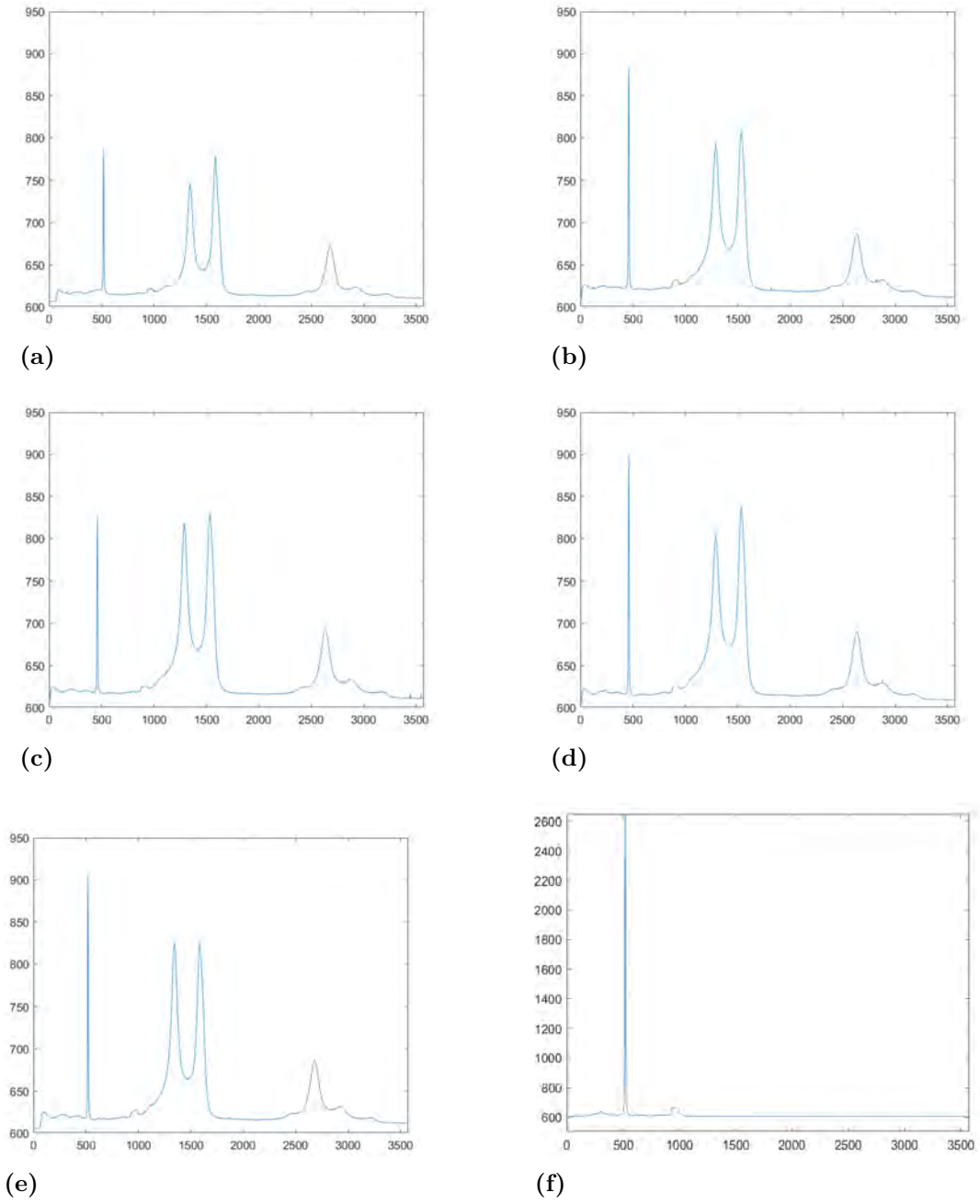


Figure 4.7: Mean Raman spectra of annealed networks.
Ni/CNT networks thermally treated at 900 C (a) 0 min (b) 2 min (c) 4 min (d) 8 min (e) 20 min. (f) shows the bakground Si substrate spectra.

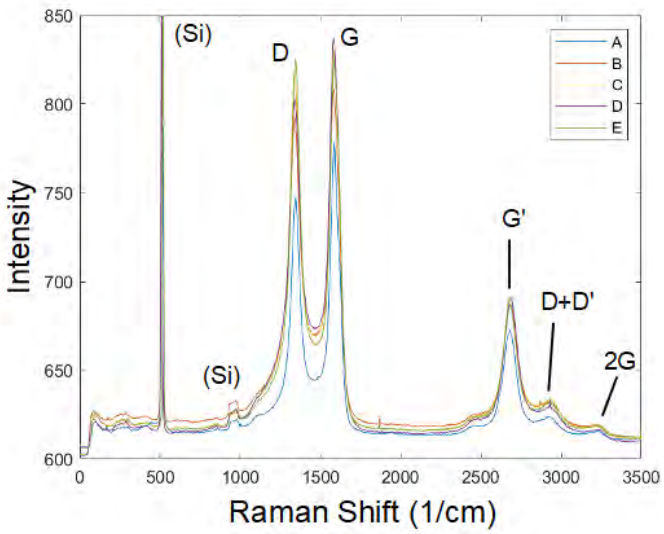


Figure 4.8: Comparison of the mean Raman spectra.
Comparison between the obtained Raman spectras where the peaks are labelled. The features of the Si substrate are noted.

When comparing the mean value spectra, a significant difference can be found. Peak D seams to increase in intensity for longer annealing times. This is the peak corresponding to disorder in the carbon hexagonal pattern, like can be seen for damaged graphene or single walled nanohorns in Figure 3.3. A detailed image of the mean peak intensities are presented in Figure 4.9. Note that there are a general, overall intensity variance amongst the samples.

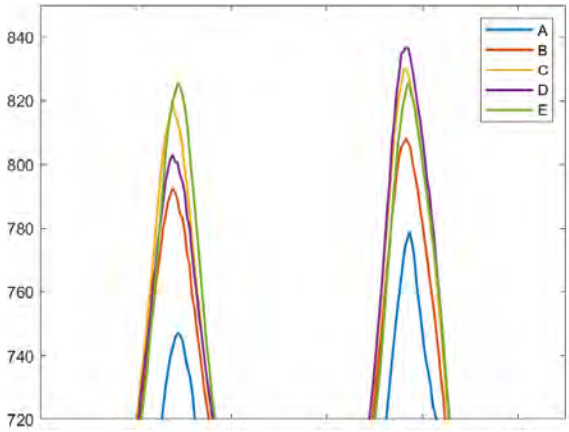


Figure 4.9: Close-up of peaks.
Comparison of peak intensity difference.

To further study the trend, a statistical line diagram of the D-peak intensity have been generated. It is shown in Figure 4.11, where the range and mean values of the D peak intensity is shown for each annealing time, as a fraction of the G peak intensity. How this fraction is calculated is explained in Figure 4.10.

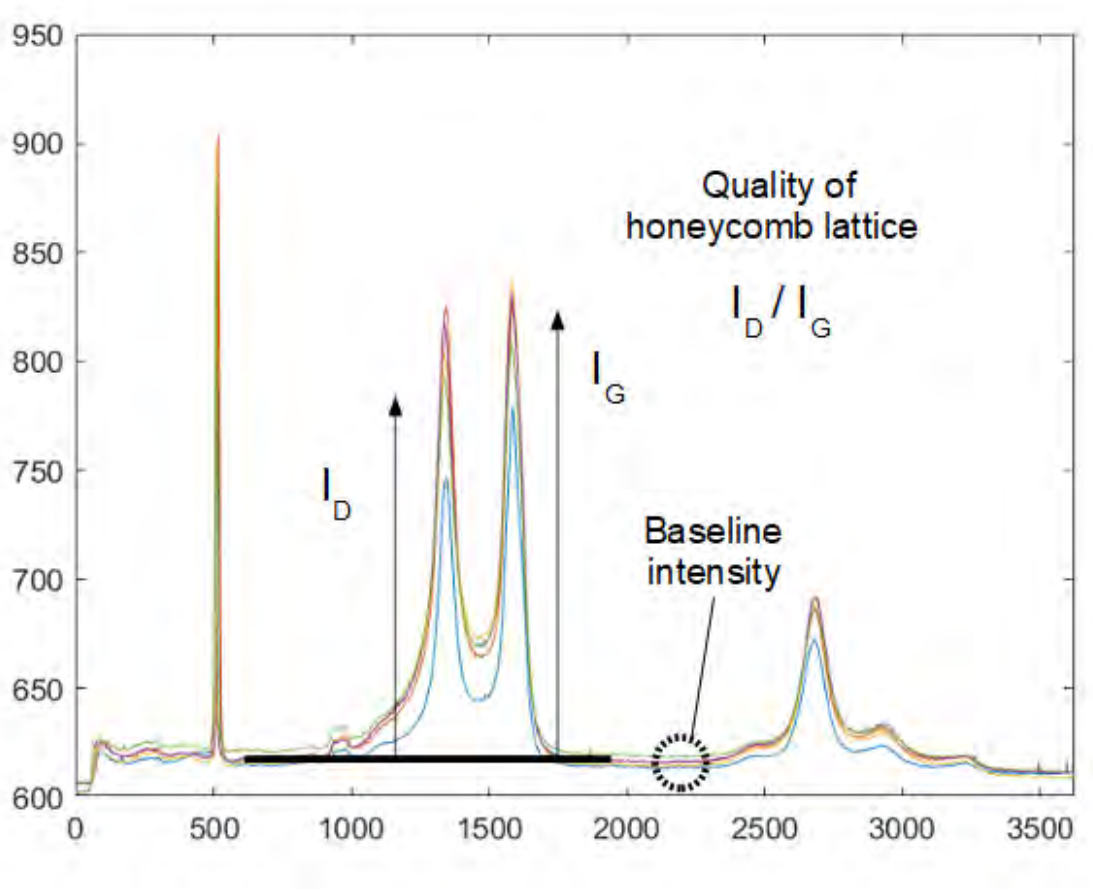


Figure 4.10: Ratio indicating honeycomb lattice quality
Comparing the height of the D and G peaks on the Raman spectrum gives an indication of the overall quality of the molecular structure of the substrate.

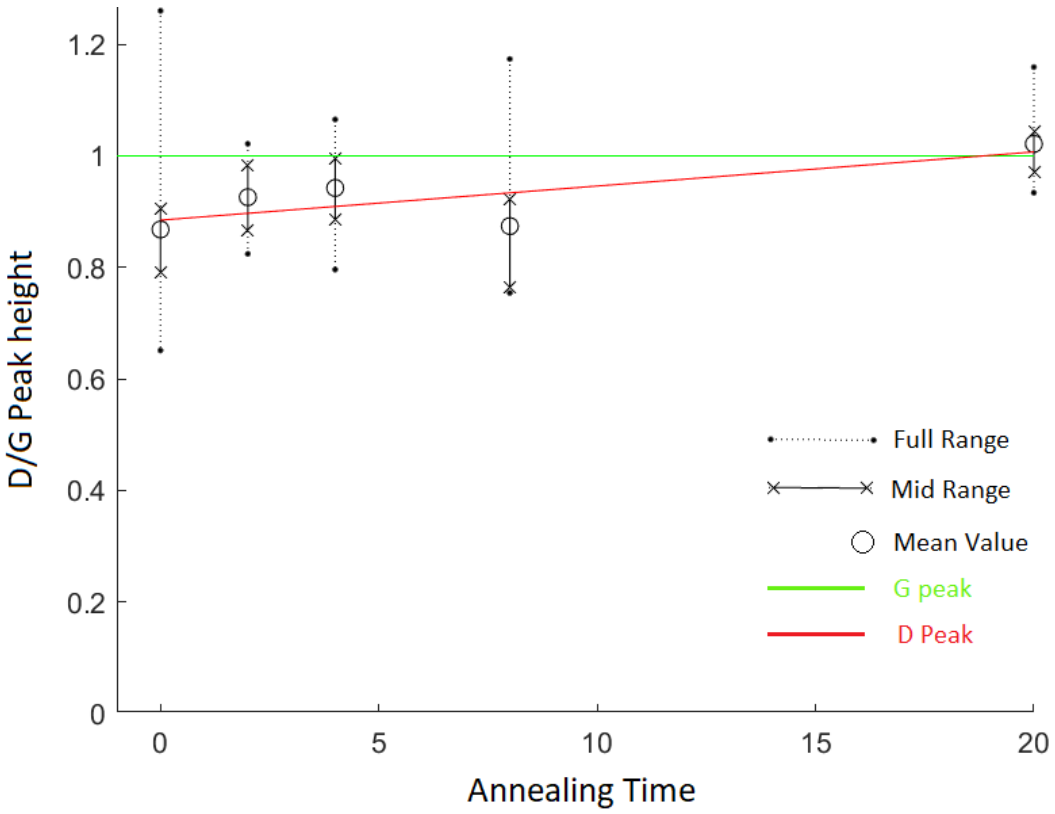


Figure 4.11: D peak height of samples
Here, a version of a box plot is used to visualize the increase of the D Peak height compared to the G peak. The full range of measurements for each sample is shown, along with the 2nd and 3rd quartile range. The mean values are plotted and used to obtain a linearly fitted graph. Note that the red D-peak line in the graph is the same as the the I_D/I_G quality indication value for the hexagonal pattern in the structure.

4.4 Simulation Output

4.4.1 Junction Visualization

As described in section 3.4.3, by logging the electron position at each step of the junction transition, for all simulations, a probability map were plotted. This map indicates where the probability is largest to find an electron at a random time of a transition, and it can be seen in figure 4.12. Note that the probability is scaled to the power of 1/3 in order to obtain a map that is easier to read. It is interesting to note that there is a probability for the electron to tunnel back from the second CNT wall to the original wall after the first transition, which lowers the tunneling effectiveness even further than otherwise would be the case.

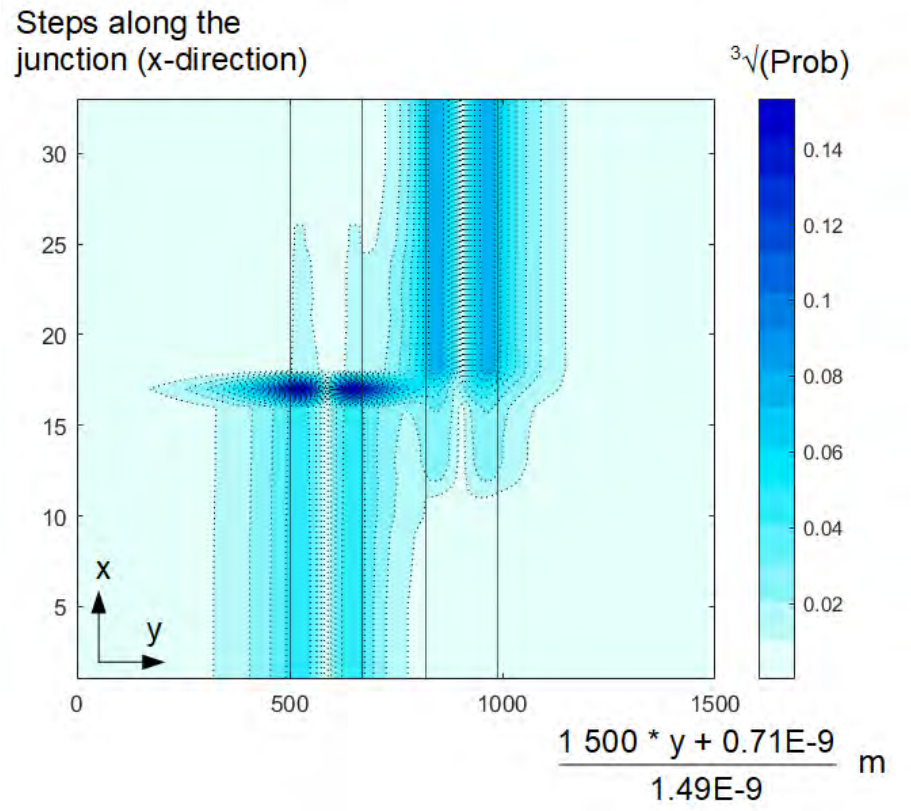


Figure 4.12: Probability map of electron position in junction.
After 100 simulations of an electron crossing the junction, the resulting probability to find the electron at all coordinates were generated.

4.4.2 Calculated Tunneling Resistance

To approximate the impact of tunneling resistance on a thin film, consider an abstracted CNT mesh in a single layer, where electrons are transported along individual routes. Each route consist of N junctions in series, and there are N routes through the mesh. This supposed idealization is visualized in Figure 4.13. The increased

resistance of a junction due to tunneling can then be used to calculate the total resistance relative to a mesh without tunneling.

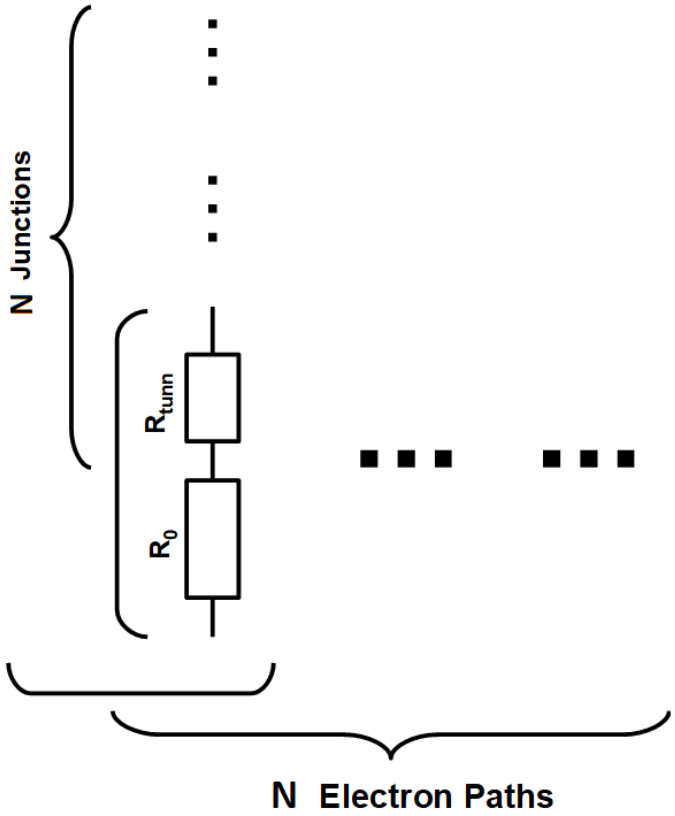


Figure 4.13: Idealized structure of CNT network resistance junctions.
An theoretical network is used to approximate the effect of tunneling resistance. Electrons are assumed to travel along N separate paths in the network. Each path consists of N junctions, where the standard CNT resistance and the additional tunneling resistance are present.

According to the simulation output, the average time it takes for an electron to pass through the junction is around $T_{avg} = 81$ time steps (TSs). The simulated value will vary somewhat each time it is run, but a value between 81 and 82 was found to be most common after 10 iterations of the Matlab script. This corresponds to a step based current of $I_{avg} = 1/81$ electrons/TSs. Considering that the transition time for a single nanotube over the same distance would be $T_0 = 33$ TSs, the decrease of current through the junction can be calculated through:

$$I_{mod} = I_{avg}/I_0 = (1/81)/(1/33) \approx 0.41$$

Since both the junction mesh and the tunneling-free mesh would be exposed to the same bias, the resistance can be found through the common equation $U = RI$:

$$U = R_{avg} * I_{avg} = R_0 * I_0$$

The average resistance of a simulated junction is therefore:

$$R_{avg} = R_0 * I_0/I_{avg} = R_0 * I_0/(I_0 * I_{mod}) \approx R_0 * 1/0.41$$

Using the average of the junction resistance expressed in terms of the non-tunneling resistance allows us to compare the two different mesh situations as we scale up to an entire $N*N$ mesh. A route of N junctions will have a serial resistance of $N*R_{avg}$. N parallel routes would result in a total mesh resistance of:

$$R_{avg.tot} = N * R_{avg}/N \approx N * R_0 * 1/(N * 0.41) \approx 2.5R_{0.tot}$$

This result is based on approximations and simplifications, which must be taken into account when drawing any conclusions from it. If one considers the assumptions of the simulation to be sufficient for a general conclusion, it would seem that having tunneling junctions in a mesh would increase the thin film resistance significantly. An actual resistance of more than double that of a theoretical mesh of unbroken CNTs would likely warrant a survey of thin film replacements. This proposition is the reason why hybrid meshes (in the case of this thesis, a Ni/CNT mesh) would be an interesting alternative.

5
Conclusion

5.1 Result Discussion

The increase of the D peak is an encouraging indicator that carbon atoms have started to spread over the surface of the interfacing Ni particles. Considering that the surfaces of the Ni nanoparticles in practice do not have the smooth nature of a Ni-film, a certain amount of disorder in the atom configuration is expected. An oversimplified illustration of this is presented in Figure 5.1.



Figure 5.1: Visualization of an CNT/Ni-particle interaction
A basic visual illustration of how the lattice of the CNT atoms would most likely be perturbed when forced to spread over an uneven surface. Which degree of perturbation would depend on the local surface smoothness and the annealing time.

In order to consider alternative explanations of the D peak intensity increase, other studies where this effect have been observed was consulted. In one experiment, the oxidation of CNTs resulted in similar D-peak behaviour (Osswald, Havel and Gogotsi 2007) [23]. The Raman scan results laid out above is, in contrast with this oxidation study, from substrates that have been exposed to oxygen the same amount of time. When not examined, the substrates have been stored in a cupboard with a nitrogen gas flow, and when taken out from storage, all substrates have been transported together in the same atmosphere. Because of this, oxidation of the CNTs is not a probable explanation for the variance in I_D/I_G seen for the substrates.

Another source of potential D-peak increase is that the samples were damaged by the laser during the Raman spectroscopy, resulting in affected CNTs having greater lattice disruption. This is an effect that was referenced in Figure 3.3. Again, this seems implausible since all substrates were treated the same way, with the same

laser intensity and performed measuring method. That random laser damage effects would result in a seemingly increasing peak ratio for mean value graphs, where the increase corresponds to longer annealing times, is not a convincing explanation.

All in all, the results of this project is seen as a sufficient indicator that the CNT/Ni network fabrication method presented in this report is suitable as a basis for further investigation a possible hybrid material. If indeed carbon atoms are spread from the CNT structure onto the Ni-nanoparticle surfaces, this material could very well be suitable as a thermal spreading layer in microfabricated devices.

5.2 Lessons Learned

A more flexible approach to the application procedure would have been advantageous. When trying the longer nanotubes, the main argument for dismissing them as an alternative was the practical limitations concerning the pipettes that were used. The solution with the longer tubes clogged up the opening during the application step, which significantly disturbed the process. However, the networks with the longer tubes were significantly less patchy compared to the other substrates, which were an advantageous aspect. A different handling procedure should have been taken into consideration in order to circumvent the practical issues and utilise the more prevalent conglomeration of the longer tubes. Even though the networks investigated in this project were found to be too dense, having less separation of both ropes of tubes and individual strands, this could have been compensated by modifying the application procedure.

To have a more conclusive Raman investigation, with less variance in the scanning values, more points of study per substrate would have been needed. Of course, more points will always yield a better statistical data set, so the practicality of a multitude of scans needs to be taken into account in any project. In this instance, twice as many scans would perhaps have been reasonable.

Regarding the simulation performed in this thesis project, the need for approximations and adaptability when building a simulation flow was underscored on several occasions. An initial, optimistic simulation goal was scaled back on several fronts as unforeseen problems were encountered. a more realistic starting point when the coding of the simulation was initiated would have been of considerable benefit.

5.3 Further Research

Further studies of this Ni/CNT hybrid material would benefit from additional optimization of the network fabrication procedure. At the closing of this project, the networks obtained were still formed in smaller patches on the substrates. While this is a common phenomenon for this kind of practical method, larger areas of hybrid material is preferable. Moving forward, it is recommended to use nanotubes similar to the longer ones that were discounted for this project, making sure to compensate

for the increased conglomeration. In order to have a smoother application procedure, pipettes with wide openings is recommended. To have less clumping of tubes in the networks, further dissolving of the solution could be an adequate remedy.

If these, or other, changes to the fabrication process is made so that larger networks are formed, another examination technique will become a possibility. Applying pairs of electrodes on the substrates would allow for the measurement of current passing through the networks. Larger interfaces between the CNTs and the Ni-nanoparticles should be detectable as lower resistance for longer annealing times, possibly strengthening the hypothesis that carbon atoms have started to spread over the nickel surfaces.

Barring new substrates with larger networks, other characterization methods could still be implemented. The existing networks could be separated from the substrates in order to investigate them with transmission electron microscopy. This could result in visual confirmation or dismissal of the suspected interface structures. Another way to further study the meshes is to etch away the nickel. If the networks stay connected at the location of smaller Ni-particle bridges, this could be due to the carbon atoms from the opposing nanotubes now being connected to each other.

Finally, there is a possibility that carbon sheets could be grown onto the Ni-particle bridges in a second CVD process. If the CNTs starts to dissolve at the nanoparticle interface and links up with atoms congregating on the Ni-surface, the particles might not be needed in order to keep the network structure. If so, the nickel could be etched away in order to obtain a hybrid material of CNTs and irregular graphene formations, chemically bonded throughout the structure. Such a material could then be investigated for use in nanoelectrical components, such as transparent electrodes in solar cells.

Bibliography

[1] Dresselhaus, M. S., Dresselhaus, G. and Avouris, P. (2001) Carbon Nanotubes. [electronic resource]:Synthesis, Structure, Properties, and Applications. 1st ed. 2001. Springer Berlin Heidelberg (Topics in Applied Physics: 80). Available at: http://search.ebscohost.com/login.aspx?direct=true&AuthType=sso&db=cat07472a&AN=clec.SPRINGERLINK9783540399476&site=eds-live&scope=site (Accessed: 29 April 2020).

[2] Nair, R. R. et al. (2008) 'Fine structure constant defines visual transparency of graphene', Science (New York, N.Y.), 320(5881), p. 1308. doi: 10.1126/science.1156965. (Accessed: 28 April 2021).

[3] CORDIS 2012, *Networks for flexible, transparent electronic devices*, viewed 28 April 2021, <https://cordis.europa.eu/article/id/89560-networks-for-flexible-transparent-electronic-devices>.

[4] Wikipedia 2007, *Honeycomb*, viewed 28 April 2021, <https://en.wikipedia.org/wiki/Honeycomb#/media/File:Honey_comb.jpg>.

[5] This Old House 2021, *Patio and Pathway Inspiration*, viewed 28 April 2021, <https://www.thisoldhouse.com/patios/21019016/diy-pathways-and-patios>

[6] Wikipedia 2021 *Carbon nanotube*, viewed 28 April 2021, <https://en.wikipedia.org/wiki/Carbon_nanotube>

[7] University of Rome Tor Vergata, Department of physics, *Carbonlab*, viewed 28 April 2021, <http://carbonlab.roma2.infn.it>

[8] Salvetat, J.-P. (1) et al. (1999) 'Elastic and shear moduli of single-walled carbon nanotube ropes', Physical Review Letters, 82(5), pp. 944–947. doi: 10.1103/PhysRevLett.82.944. (Accessed: 28 April 2021).

[9] Nordling C, Österman J, (2006), Physics Handbook, Edition 8:15, Studentlitteratur AB, Lund, Sweden

[10] Yu et al. (2005) 'Thermal Conductance and Thermopower of an Individual Single-Wall Carbon Nanotube', Nano Letters, 5(9), pp. 1842–1846. Available at: https://search.ebscohost.com/login.aspx?direct=true&AuthType=sso&db=edo&AN=20142011&site=eds-live&scope=site. (Accessed: 28 April 2021).

[11] Prasek, J. et al. (2011) 'Methods for carbon nanotubes synthesis-review', JOURNAL OF MATERIALS CHEMISTRY, 21(40), pp. 15872–15884. doi: 10.1039/c1jm12254a. (Accessed: 28 April 2021)

[12] Postma, H. W. C. et al. (2000) 'Electrical transport through carbon nanotube junctions created by mechanical manipulation'. doi: 10.1103/PhysRevB.62.R10653. (Accessed: 28 April 2021).

[13] Fuhrer MS et al. (2000) 'Crossed nanotube junctions', Science (New York, N.Y.), 288(5465), pp. 494–497. Available at:

http://search.ebscohost.com/login.aspx?direct=true&AuthType=sso&db=cmedm&AN=10775104&site=eds-live&scope=site (Accessed: 28 April 2021).

[14] Chen et al. (2003) 'Bulk Separative Enrichment in Metallic or Semiconducting Single-Walled Carbon Nanotubes', Nano Letters, 3(9), p. 1245. Available at: https://search.ebscohost.com/login.aspx?direct=true&db=edo&AN=10816330&site=eds-live&scope=site (Accessed: 28 April 2021).

[15] Lee et al. (2004) 'Single Wall Carbon Nanotubes for p-Type Ohmic Contacts to GaN Light-Emitting Diodes', Nano Letters, 4(5), pp. 911–914. Available at: https://search.ebscohost.com/login.aspx?direct=true&db=edo&AN=13131226&site=eds-live&scope=site (Accessed: 28 April 2021).

[16] Pasquier, A. D. et al. (2005) 'Conducting and transparent single-wall carbon nanotube electrodes for polymer-fullerene solar cells', Applied Physics Letters, 87(20), pp. 1–3. doi: 10.1063/1.2132065. (Accessed: 28 April 2021).

[17] Jia, L.-C. (1) et al. (2017) 'High Strain Tolerant EMI Shielding Using Carbon Nanotube Network Stabilized Rubber Composite', Advanced Materials Technologies, 2(7). doi: 10.1002/admt.201700078. (Accessed: 28 April 2021).

[18] Duzynska, A. (1) et al. (2015) 'Temperature-dependent thermal properties of single-walled carbon nanotube thin films', Applied Physics Letters, 106(18). doi: 10.1063/1.4919792. (Accessed: 28 April 2021).

[19] Kis, A. et al. (2004) 'Reinforcement of single-walled carbon nanotube bundles by intertube bridging', Nature materials, 3(3), pp. 153–157. doi: 10.1038/nmat1076. (Accessed: 28 April 2021).

[20] Haruyama, J. et al. (2011) 'Superconductivity in Boron-Doped Carbon Nanotubes', Journal of Superconductivity and Novel Magnetism, 24(1–2), p. 111. Available at: https://search.ebscohost.com/login.aspx?direct=true&db=edsgao&AN=edsgcl.254593316&site=eds-live&scope=site (Accessed: 28 April 2021).

[21] Lahiri, J. et al. (2011) 'Graphene growth and stability at nickel surfaces', NEW JOURNAL OF PHYSICS, 13. doi: 10.1088/1367-2630/13/2/025001. (Accessed: 28 April 2021).

[22] Dresselhaus, M. S. et al. (2010) 'Perspectives on Carbon Nanotubes and Graphene Raman Spectroscopy', NANO LETTERS, 10(3), pp. 751–758. doi: 10.1021/nl904286r. (Accessed: 30 April 2021)

[23] Osswald, S., Havel, M. and Gogotsi, Y. (2007) 'Monitoring oxidation of multiwalled carbon nanotubes by Raman spectroscopy', JOURNAL OF RAMAN SPECTROSCOPY, 38(6), pp. 728–736. doi: 10.1002/jrs.1686. (Accessed: 30 April 2021)

A

Appendix 1

This is the Matlab code used to simulate a CNT-CNT junction electron crossing.

```
%Pregenerated Matrixes
w_barr_vec=zeros(4,1);
Amp_mat_1LHS=zeros(7,2);
Amp_mat_1RHS=zeros(7,2);
T_mat=zeros(7,2);
%
%Defining Set Potential Values
w_well=0.335*10^-9/2; %m, well width
dist_max=1.5*w_well;%max tube distance
dist_min=0.9*w_well;%min tube distance
var_dist=(dist_min-dist_max)/3;%steps in distance
E_well=1300*1.60*10^-19; %J, well height
L=0.5*10^-9; %margin left right
U_app=370*1.60*10^-19; %applied voltage
E_well_LHS=E_well-U_app/2; %LHS well potential
E_well_RHS=E_well+U_app/2; %RHS well potential
%
%Standard values
m_e=9.12*10^-31; %kg, electron mass
h_bar=6.63*10^-34; %J/Hz, planck's constant
w_barr_max=dist_max;
%
%plot equation for initial guess LHS
E_e_first = -E_well_LHS*(0/100);
E_e_guess = -E_well_LHS:10^-19:E_e_first;
alpha = sqrt(2*m_e*(E_well_LHS+E_e_guess)./h_bar^2);
beta = sqrt(-2*m_e.*(E_e_guess)/2/h_bar^2);
phi = alpha.*(w_well/2);
neta = beta.*(w_well/2);
gamma = sqrt(2*m_e*E_well_LHS*(w_well/2)^2/h_bar^2);
f_neta_1 = sqrt(gamma^2-phi.^2);
f_neta_2 = phi.*tan(phi);
f_neta_3 = -phi.*cot(phi);
%
figure
plot(E_e_guess,f_neta_1-f_neta_2,E_e_guess,f_neta_1-f_neta_3);
axis([-E_well_LHS E_e_first 0 5]);
ELHS_approx=-3.64*10^-17;

%find approximation of beta and alpha LHS
beta_approx_LHS = sqrt(-2*m_e*ELHS_approx/h_bar^2);
alpha_approx_LHS = sqrt(2*m_e*(E_well_LHS+ELHS_approx)./h_bar^2);

%plot equation for initial guess RHS
E_e_first = -E_well_RHS*(0/100);
E_e_guess = -E_well_RHS:10^-19:E_e_first;
alpha = sqrt(2*m_e*(E_well_RHS+E_e_guess)./h_bar^2);
beta = sqrt(-2*m_e.*(E_e_guess)/2/h_bar^2);
phi = alpha.*(w_well/2);
neta = beta.*(w_well/2);
gamma = sqrt(2*m_e*E_well_RHS*(w_well/2)^2/h_bar^2);
f_neta_1 = sqrt(gamma^2-phi.^2);
```

1

Figure A.1

```
f_neta_2 = phi.*tan(phi);
f_neta_3 = -phi.*cot(phi);
%
figure
plot(E_e_guess,f_neta_1-f_neta_2,E_e_guess,f_neta_1-f_neta_3);
axis([-E_well_RHS E_e_first 0 5]);
ERHS_approx=-7.62*10^-17;
%
%find approximation of beta and alpha RHS
beta_approx_RHS = sqrt(-2*m_e*ERHS_approx/h_bar^2);
alpha_approx_RHS = sqrt(2*m_e*(E_well_RHS+ERHS_approx)./h_bar^2);
%
for i=0:1:3
%Defining Variable Potential Values
w_barr=dist_max+i*var_dist; %nm, barrier width

%y-axis
y(i+1,:)=-(w_well+L):10^-10:(w_barr_max+w_well+L);

%plot equation for initial guess LHS
E_e_first = -E_well_LHS*(0/100);

%system regions
y1=-(w_well+L):10^-12:-(w_well);
y2=-(w_well):10^-12:0;
y3=0:10^-12:w_barr;
y4=w_barr:10^-12:(w_barr+w_well);
y5=(w_barr+w_well):10^-12:(w_barr+w_well+L);
%
%combined wave functions LHS
f1=exp(beta_approx_LHS.*(y1+w_well/2));
f2=sin(alpha_approx_LHS.*(y2+w_well/2));
f3=-exp(-beta_approx_LHS.*(y3+w_well/2));
%Continuous
C1=f2(1)/f1(end);
f1=f1*C1;
f3=f3*C1;
%
%interface
y_diff=atan(beta_approx_LHS/alpha_approx_LHS)/alpha_approx_LHS...
    -y3(end)+w_barr;
f5=-sin(alpha_approx_LHS.*(y_diff+y4-(w_well/2+w_barr)));
C2=f3(end)/f5(1);
%
%starting wave functions RHS
f6=exp(-beta_approx_LHS.*(y_diff+y5-(w_well/2+w_barr)));
f5=C2*f5;
%f4=amp*-exp(beta_approx_LHS.*(y_diff+y3-(w_well/2+w_barr)));
%Continuous
C3=f5(end)/f6(1);
f6=f6*C3;
%
%
%plotting graphs
```

2

Figure A.2

```
figure
hold on
%Potential Lines
xline(y1(1));
xline(y1(end));
xline(y2(end));
xline(y3(end));
xline(y4(end));
xline(y5(end));
plot(y1,f1)
plot(y2,f2)
plot(y3,f3)
%plot(y3,f4)
plot(y4,f5)
plot(y5,f6)

%
%probability amplitude
p1=f1.^2;
p2=f2.^2;
p3=f3.^2;
p5=f5.^2;
p6=f6.^2;
%
%Normalized
A_1LHS = sum(p1)+sum(p2)+sum(p3)+sum(p5)+sum(p6);
p1=p1/A_1LHS;
p2=p2/A_1LHS;
p3=p3/A_1LHS;
p5=p5/A_1LHS;
p6=p6/A_1LHS;
%Check
A_Norm_1LHS = sum(p1)+sum(p2)+sum(p3)+sum(p5)+sum(p5);
%
figure
hold on
%Potential Lines
xline(y1(1));
xline(y1(end));
xline(y2(end));
xline(y3(end));
xline(y4(end));
xline(y5(end));
plot(y1,p1)
plot(y2,p2)
plot(y3,p3)
plot(y4,p5)
plot(y5,p6)
%
%combined wave functions RHS
f7=exp(beta_approx_RHS.*(y1+w_well/2));
f8=sin(alpha_approx_RHS.*(y2+w_well/2));
f9=-exp(-beta_approx_RHS.*(y3+w_well/2));
%Continuous
```

3

Figure A.3

```
C4=f8(1)/f7(end);
f7=f7*C4;
f9=f9*C4;
%
%interface
y_diff=atan(beta_approx_RHS/alpha_approx_RHS)/alpha_approx_RHS...
    -y3(end)+w_barr;
f11=-sin(alpha_approx_RHS.*(y_diff+y4-(w_well/2+w_barr)));
C5=f9(end)/f11(1);
%
%starting wave functions RHS
f12=exp(-beta_approx_RHS.*(y_diff+y5-(w_well/2+w_barr)));
f11=C5*f11;
%f4=amp*-exp(beta_approx_LHS.*(y_diff+y3-(w_well/2+w_barr)));
%Continuous
C6=f11(end)/f12(1);
f12=f12*C6;
%
%
%plotting graphs
figure
hold on
%Potential Lines
xline(y1(1));
xline(y1(end));
xline(y2(end));
xline(y3(end));
xline(y4(end));
xline(y5(end));
plot(y1,f7)
plot(y2,f8)
plot(y3,f9)
%plot(y3,f10)
plot(y4,f11)
plot(y5,f12)
%
%probability amplitude
p7=f7.^2;
p8=f8.^2;
p9=f9.^2;
p11=f11.^2;
p12=f12.^2;
%
%Normalized
A_1RHS = sum(p7)+sum(p8)+sum(p9)+sum(p11)+sum(p12);
p7=p7/A_1RHS;
p8=p8/A_1RHS;
p9=p9/A_1RHS;
p11=p11/A_1RHS;
p12=p12/A_1RHS;
%Check
A_Norm_1RHS = sum(p7)+sum(p8)+sum(p9)+sum(p11)+sum(p12);
%
figure
```

4

Figure A.4

```
hold on
%Potential Lines
xline(y1(1));
xline(y1(end));
xline(y2(end));
xline(y3(end));
xline(y4(end));
xline(y5(end));
plot(y1,p7)
plot(y2,p8)
plot(y3,p9)
plot(y4,p11)
plot(y5,p12)
%
f_LHS_1(i+1,:)=f1;
f_LHS_2(i+1,:)=f2;
f_LHS_3(i+1,1:length(f3))=f3(1,1:length(f3));
f_LHS_4(i+1,:)=f5;
f_LHS_5(i+1,:)=f6;
%
f_RHS_1(i+1,:)=f7;
f_RHS_2(i+1,:)=f8;
f_RHS_3(i+1,1:length(f9))=f9(1:1:length(f9));
f_RHS_4(i+1,:)=f11;
f_RHS_5(i+1,:)=f12;
%
%Amplitude Matrix
w_barr_vec(i+1,1)=w_barr;
Amp_mat_1LHS(i+1,1)=max(p2);
Amp_mat_1LHS(i+1,2)=max(p5);
Amp_mat_1LHS(7-i,1)=Amp_mat_1LHS(i+1,1);
Amp_mat_1LHS(7-i,2)=Amp_mat_1LHS(i+1,2);
Amp_mat_1RHS(i+1,1)=max(p8);
Amp_mat_1RHS(i+1,2)=max(p11);
Amp_mat_1RHS(7-i,1)=Amp_mat_1RHS(i+1,1);
Amp_mat_1RHS(7-i,2)=Amp_mat_1RHS(i+1,2);
end
T_mat(:,1)=Amp_mat_1LHS(:,2)/Amp_mat_1LHS(1,1);
T_mat(:,2)=Amp_mat_1RHS(:,2)/Amp_mat_1RHS(1,1);
%Assumed limit of tunneling
Prob_vecLHS=zeros(9,1);
Prob_vecLHS(2:8)=T_mat(:,1);
Prob_vecRHS=zeros(9,1);
Prob_vecRHS(2:8)=T_mat(:,2);
%
%LHS
Prob_curve_LHS=zeros(1,33);
for i=1:1:8
    values=Prob_vecLHS(i):(Prob_vecLHS(i+1)-...
        Prob_vecLHS(i))/4:Prob_vecLHS(i+1)-(Prob_vecLHS(i+1)-...
        Prob_vecLHS(i))/4;
    minimum=4*i-3;
    maximum=4*i;
    Prob_curve_LHS(1,minimum:maximum)=values;
```

5

Figure A.5

```
end
%RHS
Prob_curve_RHS=zeros(1,33);
for i=1:1:8
    values=Prob_vecRHS(i):(Prob_vecRHS(i+1)-...
        Prob_vecRHS(i))/4:Prob_vecRHS(i+1)-(Prob_vecRHS(i+1)-...
        Prob_vecRHS(i))/4;
    minimum=4*i-3;
    maximum=4*i;
    Prob_curve_RHS(1,minimum:maximum)=values;
end
%
x_vec=1:0.25:9;
%
%exponential interpolation of tunneling probability
x_Exp_low=1:0.25:5;
Exp_CLHS=Prob_vecLHS(5,1)/5^3.3;
Exp_LHS_low=Exp_CLHS.*(x_Exp_low).^3.3;
%
x_Exp_high=5:0.25:9;
for i=1:1:length(Exp_LHS_low)
Exp_LHS_high(1,i)=Exp_LHS_low(1,length(Exp_LHS_low)+1-i);
end
%
figure
hold on
plot(x_vec,Prob_curve_LHS,x_Exp_low,Exp_LHS_low,x_Exp_high,Exp_LHS_high)
%
Exp_CRHS=Prob_vecRHS(5,1)/5^5;
Exp_RHS_low=Exp_CRHS.*(x_Exp_low).^5;
%
for i=1:1:length(Exp_LHS_low)
Exp_RHS_high(1,i)=Exp_RHS_low(1,length(Exp_LHS_low)+1-i);
end
%
figure
hold on
plot(x_vec,Prob_curve_RHS,x_Exp_low,Exp_RHS_low,x_Exp_high,Exp_RHS_high)
%
Exp_approx_T(1:length(x_Exp_low),1)=Exp_LHS_low(1,1:length(x_Exp_low));
Exp_approx_T(length(x_Exp_low)+1:length(x_Exp_low)*2-1,1)=...
    Exp_LHS_high(1,2:length(x_Exp_low));
Exp_approx_T(1:length(x_Exp_low),2)=Exp_RHS_low(1,1:length(x_Exp_low));
Exp_approx_T(length(x_Exp_low)+1:length(x_Exp_low)*2-1,2)=...
    Exp_RHS_high(1,2:length(x_Exp_low));
%
pos_mat=zeros(length(x_vec),2);
pos_mat(length(x_vec),1)=1;
pos_mat_start=pos_mat;
%
iterations=100;
Coll_timestamp=zeros(33,2,101,iterations);
Pass_map=zeros(33,2,2);
Coll_iter=zeros(2,1);
```

6

Figure A.6

```
Coll_Pass_map=zeros(33,2);
for i=1:1:iterations
    j=1;
    pos_mat=pos_mat_start;
    Sum_pos=pos_mat_start;
    Timestamp=zeros(33,2);
while pos_mat(1,2) < 1 && j < 300
    j=j+1;
    [row,col] = find(pos_mat);
    Tunn_Prob=Exp_approx_T(row,col);
    V=rand;
    if col < 2
        col2=2;
    else
        col2=1;
    end
    %
    if V < Tunn_Prob
        pos_mat(row,col)=0;
        pos_mat(row,col2)=1;
    else
    end
    %
    if sum(pos_mat(1:16,1)) > 0
        pos_mat(row+1,:)=pos_mat(row,:);
        pos_mat(row,:)=zeros(1,2);
    elseif pos_mat(17,1) > 0
    else
        pos_mat(row-1,:)=pos_mat(row,:);
        pos_mat(row,:)=zeros(1,2);
    end
    %
    Sum_pos=Sum_pos+pos_mat;
    if j > 300
        break
    end
    Timestamp(:,:,j)=pos_mat;
    iter=j-1;
end
    Timestamp(:,:,1)=pos_mat_start;
    Coll_iter(i,1)=iter;
    Coll_timestamp(1:33,1:2,1:iter,i)=Timestamp(1:33,1:2,1:iter);
    Pass_map(:,:,i)=Sum_pos;
    Coll_Pass_map=Coll_Pass_map+Sum_pos;
end
%
Junction_prob(1:33,1:2)=Coll_Pass_map(1:33,1:2)./sum(Coll_Pass_map);
%
y_max=y(1,:);
y_glob=y_max(1)-40*10^-12:10^-12:y_max(end)+39*10^-12;
%
for j=1:1:4
        values_LHS=0;
        values_RHS=0;
```

7

Figure A.7

```
            missing_LHS=0;
            missing_RHS=0;
        for i=1:1:length(f_LHS_3(j,:))
            %
        if f_LHS_3(j,i) > 0
            values_LHS=values_LHS+1;
        else
            missing_LHS=missing_LHS+1;
        end
        %
        if f_RHS_3(j,i) > 0
            values_RHS=values_RHS+1;
        else
            missing_RHS=missing_RHS+1;
        end
        end
        val_LHS(j)=values_LHS;
        val_RHS(j)=values_RHS;
        miss_LHS(j)=missing_LHS;
        miss_RHS(j)=missing_RHS;
end
%
%
%Rescaling of barrier functions
resc_barr_w=val_LHS(4);
for n=1:1:4
for i=1:1:resc_barr_w
a=val_LHS(n);
b=a/val_LHS(4);
f_LHS_3_rescale(n,i)=f_LHS_3(n,round(i*b));
f_RHS_3_rescale(n,i)=f_RHS_3(n,round(i*b));
end
end
%
%
%LHS collected functions
%wave functions
f_LHS_A1=[f_LHS_1(1,:),f_LHS_2(1,:),f_LHS_3_rescale(1,:),...
    f_LHS_4(1,:),f_LHS_5(1,:)];
f_LHS_A2=[f_LHS_1(2,:),f_LHS_2(2,:),f_LHS_3_rescale(2,:),...
    f_LHS_4(2,:),f_LHS_5(2,:)];
f_LHS_A3=[f_LHS_1(3,:),f_LHS_2(3,:),f_LHS_3_rescale(3,:),...
    f_LHS_4(3,:),f_LHS_5(3,:)];
f_LHS_A4=[f_LHS_1(4,:),f_LHS_2(4,:),f_LHS_3_rescale(4,:),...
    f_LHS_4(4,:),f_LHS_5(4,:)];
%
y_glob_resc(1,1:length(f_LHS_A1))=y_glob(1,1:length(f_LHS_A1));
%
%Probability
P_LHS_A1=f_LHS_A1.^2;
P_LHS_A2=f_LHS_A2.^2;
P_LHS_A3=f_LHS_A3.^2;
P_LHS_A4=f_LHS_A4.^2;
%
```

8

Figure A.8

```
%Normalized
P_LHS_A1_norm=P_LHS_A1/sum(P_LHS_A1);
P_LHS_A2_norm=P_LHS_A2/sum(P_LHS_A2);
P_LHS_A3_norm=P_LHS_A3/sum(P_LHS_A3);
P_LHS_A4_norm=P_LHS_A4/sum(P_LHS_A4);
%
%RHS collected functions
%wave functions
f_RHS_A1=[f_RHS_1(1,:),f_RHS_2(1,:),f_RHS_3_rescale(1,:),...
    f_RHS_4(1,:),f_RHS_5(1,:)];
f_RHS_A2=[f_RHS_1(2,:),f_RHS_2(2,:),f_RHS_3_rescale(2,:),...
    f_RHS_4(2,:),f_RHS_5(2,:)];
f_RHS_A3=[f_RHS_1(3,:),f_RHS_2(3,:),f_RHS_3_rescale(3,:),...
    f_RHS_4(3,:),f_RHS_5(3,:)];
f_RHS_A4=[f_RHS_1(4,:),f_RHS_2(4,:),f_RHS_3_rescale(4,:),...
    f_RHS_4(4,:),f_RHS_5(4,:)];
%
%probability
P_RHS_A1=f_RHS_A1.^2;
P_RHS_A2=f_RHS_A2.^2;
P_RHS_A3=f_RHS_A3.^2;
P_RHS_A4=f_RHS_A4.^2;
%
%Normalized
P_RHS_A1_norm=P_RHS_A1/sum(P_RHS_A1);
P_RHS_A2_norm=P_RHS_A2/sum(P_RHS_A2);
P_RHS_A3_norm=P_RHS_A3/sum(P_RHS_A3);
P_RHS_A4_norm=P_RHS_A4/sum(P_RHS_A4);
%
%linear approximation of probability
A=33;
%
Prob_Amp_LHS=zeros(A,length(y_glob_resc));
Prob_Amp_LHS(1,:)=P_LHS_A1_norm(1,:);
Prob_Amp_LHS(5,:)=P_LHS_A1_norm(1,:);
Prob_Amp_LHS(9,:)=P_LHS_A2_norm(1,:);
Prob_Amp_LHS(13,:)=P_LHS_A3_norm(1,:);
Prob_Amp_LHS(17,:)=P_LHS_A4_norm(1,:);
Prob_Amp_LHS(21,:)=P_LHS_A3_norm(1,:);
Prob_Amp_LHS(25,:)=P_LHS_A2_norm(1,:);
Prob_Amp_LHS(29,:)=P_LHS_A1_norm(1,:);
Prob_Amp_LHS(33,:)=P_LHS_A1_norm(1,:);
for i=2:1:4
    Prob_Amp_LHS(i,:)=Prob_Amp_LHS(1,:)*(1-0.25*(i-1))+...
        Prob_Amp_LHS(5,:)*(0.25*(i-1));
    Prob_Amp_LHS(A+1-i,:)=Prob_Amp_LHS(i,:);
end
%
for i=6:1:8
    Prob_Amp_LHS(i,:)=Prob_Amp_LHS(5,:)*(1-0.25*(i-5))+...
        Prob_Amp_LHS(9,:)*(0.25*(i-5));
    Prob_Amp_LHS(A+1-i,:)=Prob_Amp_LHS(i,:);
end
%
```

9

Figure A.9

```
for i=10:1:12
    Prob_Amp_LHS(i,:)=Prob_Amp_LHS(9,:)*(1-0.25*(i-6))+...
        Prob_Amp_LHS(13,:)*(0.25*(i-6));
    Prob_Amp_LHS(A+1-i,:)=Prob_Amp_LHS(i,:);
end
%
for i=14:1:16
    Prob_Amp_LHS(i,:)=Prob_Amp_LHS(13,:)*(1-0.25*(i-13))+...
        Prob_Amp_LHS(17,:)*(0.25*(i-13));
    Prob_Amp_LHS(A+1-i,:)=Prob_Amp_LHS(i,:);
end
%
Prob_Amp_RHS=zeros(A,length(y_glob_resc));
Prob_Amp_RHS(1,:)=P_RHS_A1_norm(1,:);
Prob_Amp_RHS(5,:)=P_RHS_A1_norm(1,:);
Prob_Amp_RHS(9,:)=P_RHS_A2_norm(1,:);
Prob_Amp_RHS(13,:)=P_RHS_A3_norm(1,:);
Prob_Amp_RHS(17,:)=P_RHS_A4_norm(1,:);
Prob_Amp_RHS(21,:)=P_RHS_A3_norm(1,:);
Prob_Amp_RHS(25,:)=P_RHS_A2_norm(1,:);
Prob_Amp_RHS(29,:)=P_RHS_A1_norm(1,:);
Prob_Amp_RHS(33,:)=P_RHS_A1_norm(1,:);
for i=2:1:4
    Prob_Amp_RHS(i,:)=Prob_Amp_RHS(1,:)*(1-0.25*(i-1))+...
        Prob_Amp_RHS(5,:)*(0.25*(i-1));
    Prob_Amp_RHS(A+1-i,:)=Prob_Amp_RHS(i,:);
end
%
for i=6:1:8
    Prob_Amp_RHS(i,:)=Prob_Amp_RHS(5,:)*(1-0.25*(i-5))+...
        Prob_Amp_RHS(9,:)*(0.25*(i-5));
    Prob_Amp_RHS(A+1-i,:)=Prob_Amp_RHS(i,:);
end
%
for i=10:1:12
    Prob_Amp_RHS(i,:)=Prob_Amp_RHS(9,:)*(1-0.25*(i-6))+...
        Prob_Amp_RHS(13,:)*(0.25*(i-6));
    Prob_Amp_RHS(A+1-i,:)=Prob_Amp_RHS(i,:);
end
%
for i=14:1:16
    Prob_Amp_RHS(i,:)=Prob_Amp_RHS(13,:)*(1-0.25*(i-13))+...
        Prob_Amp_RHS(17,:)*(0.25*(i-13));
    Prob_Amp_RHS(A+1-i,:)=Prob_Amp_RHS(i,:);
end
%
P_RHS_flipped=zeros(33,length(y_glob_resc));
%
for n=1:1:33
for i=1:1:length(y_glob_resc)
    Prob_Amp_RHS_flipped(n,i)=Prob_Amp_RHS(n,length(y_glob_resc)+1-i);
end
end
%
```


Figure A.10

X

```
Filled_cp_mat=zeros(33,length(y_glob_resc));
for i=1:1:33
    Filled_cp_mat(34-i,:)=Prob_Amp_LHS(i,:)*Junction_prob(i,1)+...
        Prob_Amp_RHS_flipped(i,:)*Junction_prob(i,2);
end
%

%Potential well lines
Y_wall_1=length(f_LHS_1(1,:));
Y_wall_2=length(f_LHS_1(1,:))+length(f_LHS_2(1,:));
Y_wall_3=length(f_LHS_1(1,:))+length(f_LHS_2(1,:))+...
    length(f_LHS_3_rescale(1,:));
Y_wall_4=length(f_LHS_1(1,:))+length(f_LHS_2(1,:))+...
    length(f_LHS_3_rescale(1,:))+length(f_LHS_4(1,:));
%
%colormap
wb_colormap=[0.9 1 0.98; 0.72 0.98 0.98; 0.54 0.96 0.98;...
    0.36 0.94 0.98; 0.18 0.92 0.98; 0 0.9 0.98; 0 0.8 0.96;...
    0 0.7 0.94; 0 0.6 0.92; 0 0.5 0.9; 0 0.4 0.88; 0 0.3 0.86;...
    0 0.2 0.84; 0 0.1 0.82; 0 0 0.8];
%
Y=1:1:length(y_glob_resc);
X=1:1:33;
Z=(Filled_cp_mat(X,Y)).^(1/3);
figure
contourf(Y,X,Z,15,':')
xline(Y_wall_1);
xline(Y_wall_2);
xline(Y_wall_3);
xline(Y_wall_4);
axis([0 1500 1 33]);
colormap(wb_colormap)
%
%
%
```

B

Appendix 2

Black Magic 1 CNT growth recipe. The different growth times are noted here, in seconds.

COMM Gases: H2, N2, C2H2
ALAR MFC1 ON 10.0 30 WARN
ALAR MFC3 ON 10.0 30 WARN
ALAR TEMP ON 10.0 60 WARN
VALV 1 OPEN
VALV 4 OPEN
WAIT PRES < 0.20
FLOW 1 ON 692
TUNE HTTC AN 500C
HEAT ON 500.0 300.0
WAIT TEMP > 495.0
WAIT TIME > 180
TUNE HTTC AN 750C
HEAT ON 700.0 0.0
FLOW 1 ON 692
FLOW 3 ON 200
WAIT TEMP > 695.0
WAIT TIME > (**35**, **175**)
FLOW 1 OFF
FLOW 3 OFF
HEAT OFF
VALV 1 OPEN
WAIT TEMP < 500.0
WAIT PRES < 0.20
FLOW 2 ON 1000
VALV 1 CLOSE
WAIT TEMP < 200.0
FLOW 2 OFF
VALV 1 OPEN
WAIT PRES < 0.20
VALV 4 CLOSE
SimuExp

C

Appendix 3

Here, the Black Magic 1 recipe used for annealing the samples is presented. The varying time intervals for annealing is noted at the proper line entry. The time inputs are in seconds, the temperatures are in Celsius.

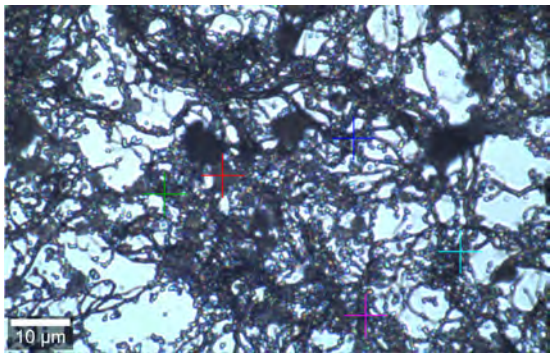
COMM Gases: H2, N2, C2H2
ALAR MFC1 ON 10.0 30 WARN
ALAR MFC3 ON 10.0 30 WARN
ALAR TEMP ON 10.0 60 WARN
VALV 1 OPEN
VALV 4 OPEN
WAIT PRES $<$ 0.20
FLOW 1 ON 692
VALV 1 CLOSE
TUNE HTTC AN 500C
HEAT ON 500.0 300.0
WAIT TEMP $>$ 495.0
TUNE HTTC Jie 2017 1000 C
HEAT ON 900.0 300.0
FLOW 1 ON 692
WAIT TEMP $>$ 885.0
WAIT TIME $>$ (**120**, **240**, **480**, **1200**)
FLOW 1 OFF
FLOW 3 OFF
HEAT OFF
VALV 1 OPEN
WAIT TEMP $<$ 500.0
WAIT PRES $<$ 0.20
FLOW 2 ON 1000
VALV 1 CLOSE
WAIT TEMP $<$ 200.0
FLOW 2 OFF
VALV 1 OPEN
WAIT PRES $<$ 0.20
VALV 4 CLOSE

D

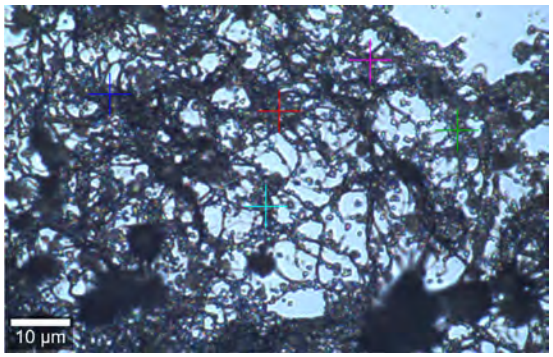
Appendix 4

These images shows the parts of the substrates where the Raman spectroscopy measurements were performed. Each substrate was investigated at two separate locations. Five points of measurements were recorded at each location. The colours corresponds to the order in which the measurements were made, therefore indicating where each data set was collected from.

The scans were made first at location a, then at location b, in the following colour order.
1) Red; 2) Blue; 3) Green; 4) Cyan; 5) Purple

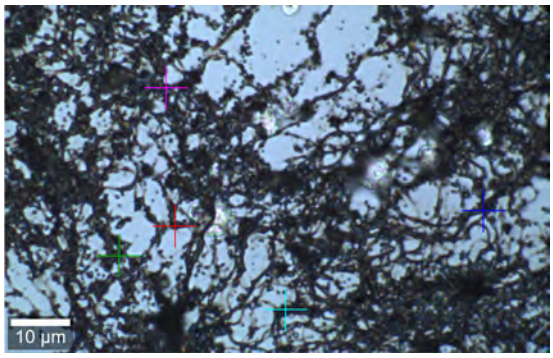


(a)

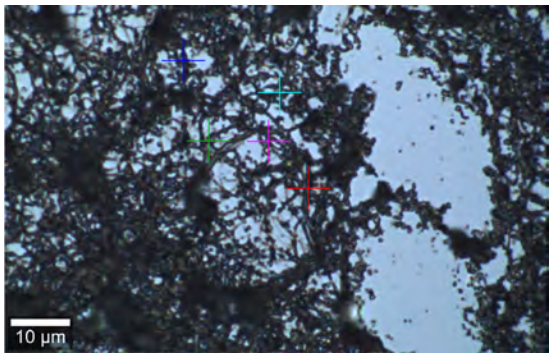


(b)

Figure D.1

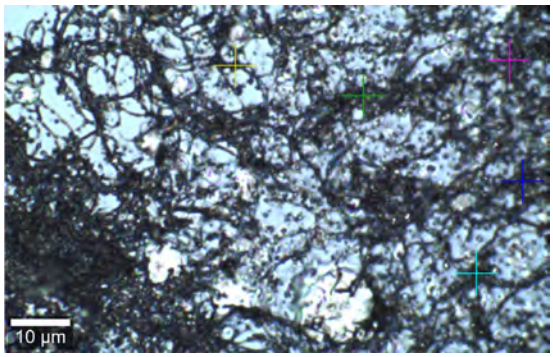


(a)

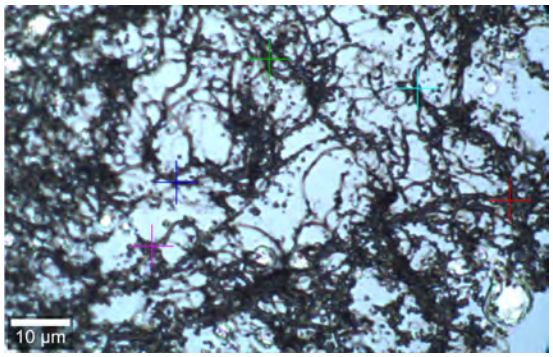


(b)

Figure D.2

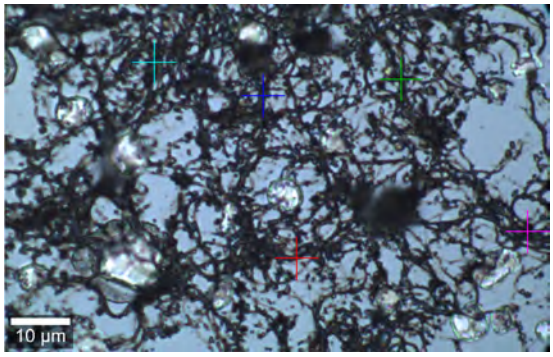


(a)

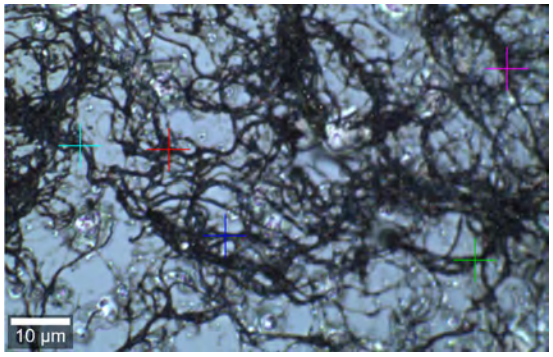


(b)

Figure D.3

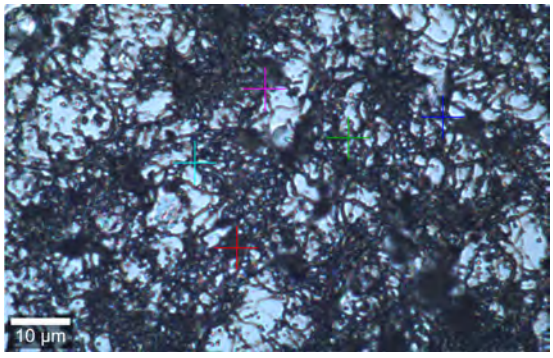


(a)

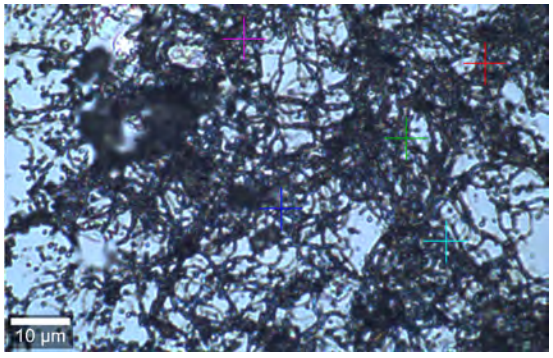


(b)

Figure D.4



(a)



(b)

Figure D.5

E

Appendix 5

This is the Matlab code used to generate the graphs from the raw Raman data.

```
%Raman spectra most annealed and not annealed samples
load('C:\Users\46737\Desktop\Examensarbete\Mätningar\David J
\X1_B_Si_014_Spec.Data 1.mat')
load('C:\Users\46737\Desktop\Examensarbete\Mätningar\David J\ascii
\X1_004_Spec.Data 1 (X-Axis).txt')
%full text shown here
% C:\Users\46737\Desktop\Examensarbete\Mätningar\David J\
%    X1_B_Si_014_Spec.Data 1.mat
% C:\Users\46737\Desktop\Examensarbete\Mätningar\David J\
%    ascii\X1_004_Spec.Data 1 (X-Axis).txt
%
x_axis=X1_004_Spec_Data_1__X_Axis_';
s_Si=X1_B_Si_014_SpecData_1.data;
plot(x_axis,s_Si)
axis([0 inf 500 inf])
saveas(gcf,'s_Si.png')
clf

load('C:\Users\46737\Desktop\Examensarbete\Mätningar\David J
\X1_004_Spec.Data 1.mat')
%full text shown here
%C:\Users\46737\Desktop\Examensarbete\Mätningar\David J\
%  X1_004_Spec.Data 1.mat
X1_A(1,:)=X1_004_SpecData_1.data;
%
load('C:\Users\46737\Desktop\Examensarbete\Mätningar\David J
\X1_005_Spec.Data 1.mat')
%full text shown here
%C:\Users\46737\Desktop\Examensarbete\Mätningar\David J\
%  X1_005_Spec.Data 1.mat
X1_A(2,:)=X1_005_SpecData_1.data;
%
load('C:\Users\46737\Desktop\Examensarbete\Mätningar\David J
\X1_006_Spec.Data 1.mat')
%full text shown here
%C:\Users\46737\Desktop\Examensarbete\Mätningar\David J\
%  X1_006_Spec.Data 1.mat
X1_A(3,:)=X1_006_SpecData_1.data;
%
load('C:\Users\46737\Desktop\Examensarbete\Mätningar\David J
\X1_007_Spec.Data 1.mat')
%full text shown here
%C:\Users\46737\Desktop\Examensarbete\Mätningar\David J\
%  X1_007_Spec.Data 1.mat
X1_A(4,:)=X1_007_SpecData_1.data;
%
load('C:\Users\46737\Desktop\Examensarbete\Mätningar\David J
\X1_008_Spec.Data 1.mat')
%full text shown here
%C:\Users\46737\Desktop\Examensarbete\Mätningar\David J\
%  X1_008_Spec.Data 1.mat
X1_A(5,:)=X1_008_SpecData_1.data;
```

1

Figure E.1

```
%
%
load('C:\Users\46737\Desktop\Examensarbete\Mätningar\David J
\X1_B_009_Spec.Data 1.mat')
%full text shown here
%C:\Users\46737\Desktop\Examensarbete\Mätningar\David J\
%  X1_B_009_Spec.Data 1.mat
X1_B(1,:)=X1_B_009_SpecData_1.data;
%
load('C:\Users\46737\Desktop\Examensarbete\Mätningar\David J
\X1_B_010_Spec.Data 1.mat')
%full text shown here
%C:\Users\46737\Desktop\Examensarbete\Mätningar\David J\
%  X1_B_010_Spec.Data 1.mat
X1_B(2,:)=X1_B_010_SpecData_1.data;
%
load('C:\Users\46737\Desktop\Examensarbete\Mätningar\David J
\X1_B_011_Spec.Data 1.mat')
%full text shown here
%C:\Users\46737\Desktop\Examensarbete\Mätningar\David J\
%  X1_B_011_Spec.Data 1.mat
X1_B(3,:)=X1_B_011_SpecData_1.data;
%
load('C:\Users\46737\Desktop\Examensarbete\Mätningar\David J
\X1_B_012_Spec.Data 1.mat')
%full text shown here
%C:\Users\46737\Desktop\Examensarbete\Mätningar\David J\
%  X1_B_012_Spec.Data 1.mat
X1_B(4,:)=X1_B_012_SpecData_1.data;
%
load('C:\Users\46737\Desktop\Examensarbete\Mätningar\David J
\X1_B_013_Spec.Data 1.mat')
%full text shown here
%C:\Users\46737\Desktop\Examensarbete\Mätningar\David J\
%  X1_B_013_Spec.Data 1.mat
X1_B(5,:)=X1_B_013_SpecData_1.data;
%
M_X1=[X1_A; X1_B];
%
for i=1:1:10
    hold on
    plot(x_axis,M_X1(i,:));
end
axis([0 inf 600 1050])
saveas(gcf,'s_X1.png')
clf

load('C:\Users\46737\Desktop\Examensarbete\Mätningar\David J
\X2_A_015_Spec.Data 1.mat')
%full text shown here
%C:\Users\46737\Desktop\Examensarbete\Mätningar\David J\
%  X2_A_015_Spec.Data 1.mat
X2_A(1,:)=X2_A_015_SpecData_1.data;
%
```

2

Figure E.2

```
load('C:\Users\46737\Desktop\Examensarbete\Mätningar\David J
\X2_A_016_Spec.Data 1.mat')
%full text shown here
%C:\Users\46737\Desktop\Examensarbete\Mätningar\David J\
%  X2_A_016_Spec.Data 1.mat
X2_A(2,:)=X2_A_016_SpecData_1.data;
%
load('C:\Users\46737\Desktop\Examensarbete\Mätningar\David J
\X2_A_017_Spec.Data 1.mat')
%full text shown here
%C:\Users\46737\Desktop\Examensarbete\Mätningar\David J\
%  X2_A_017_Spec.Data 1.mat
X2_A(3,:)=X2_A_017_SpecData_1.data;
%
load('C:\Users\46737\Desktop\Examensarbete\Mätningar\David J
\X2_A_018_Spec.Data 1.mat')
%full text shown here
%C:\Users\46737\Desktop\Examensarbete\Mätningar\David J\
%  X2_A_018_Spec.Data 1.mat
X2_A(4,:)=X2_A_018_SpecData_1.data;
%
load('C:\Users\46737\Desktop\Examensarbete\Mätningar\David J
\X2_A_019_Spec.Data 1.mat')
%full text shown here
%C:\Users\46737\Desktop\Examensarbete\Mätningar\David J\
%  X2_A_019_Spec.Data 1.mat
X2_A(5,:)=X2_A_019_SpecData_1.data;
%
%
load('C:\Users\46737\Desktop\Examensarbete\Mätningar\David J
\X2_C_025_Spec.Data 1.mat')
%full text shown here
%C:\Users\46737\Desktop\Examensarbete\Mätningar\David J\
%  X2_C_025_Spec.Data 1.mat
X2_B(1,:)=X2_C_025_SpecData_1.data;
%
load('C:\Users\46737\Desktop\Examensarbete\Mätningar\David J
\X2_C_026_Spec.Data 1.mat')
%full text shown here
%C:\Users\46737\Desktop\Examensarbete\Mätningar\David J\
%  X2_C_026_Spec.Data 1.mat
X2_B(2,:)=X2_C_026_SpecData_1.data;
%
load('C:\Users\46737\Desktop\Examensarbete\Mätningar\David J
\X2_C_027_Spec.Data 1.mat')
%full text shown here
%C:\Users\46737\Desktop\Examensarbete\Mätningar\David J\
%  X2_C_027_Spec.Data 1.mat
X2_B(3,:)=X2_C_027_SpecData_1.data;
%
load('C:\Users\46737\Desktop\Examensarbete\Mätningar\David J
\X2_C_028_Spec.Data 1.mat')
%full text shown here
%C:\Users\46737\Desktop\Examensarbete\Mätningar\David J\
```

3

Figure E.3

```
%  X2_C_028_Spec.Data 1.mat
X2_B(4,:)=X2_C_028_SpecData_1.data;
%
load('C:\Users\46737\Desktop\Examensarbete\Mätningar\David J
\X2_C_029_Spec.Data 1.mat')
%full text shown here
%C:\Users\46737\Desktop\Examensarbete\Mätningar\David J\
%  X2_C_029_Spec.Data 1.mat
X2_B(5,:)=X2_C_029_SpecData_1.data;
%
M_X2=[X2_A; X2_B];
%
for i=1:1:10
    hold on
    plot(x_axis,M_X2(i,:));
end
axis([0 inf 600 1050])
saveas(gcf,'s_X2.png')
clf

load('C:\Users\46737\Desktop\Examensarbete\Mätningar\David J
\X3_A_037_Spec.Data 1.mat')
%full text shown here
%C:\Users\46737\Desktop\Examensarbete\Mätningar\David J\
%  X3_A_037_Spec.Data 1.mat
X3_A(1,:)=X3_A_037_SpecData_1.data;
%
load('C:\Users\46737\Desktop\Examensarbete\Mätningar\David J
\X3_A_038_Spec.Data 1.mat')
%full text shown here
%C:\Users\46737\Desktop\Examensarbete\Mätningar\David J\
%  X3_A_038_Spec.Data 1.mat
X3_A(2,:)=X3_A_038_SpecData_1.data;
%
load('C:\Users\46737\Desktop\Examensarbete\Mätningar\David J
\X3_A_039_Spec.Data 1.mat')
%full text shown here
%C:\Users\46737\Desktop\Examensarbete\Mätningar\David J\
%  X3_A_039_Spec.Data 1.mat
X3_A(3,:)=X3_A_039_SpecData_1.data;
%
load('C:\Users\46737\Desktop\Examensarbete\Mätningar\David J
\X3_A_042_Spec.Data 1.mat')
%full text shown here
%C:\Users\46737\Desktop\Examensarbete\Mätningar\David J\
%  X3_A_042_Spec.Data 1.mat
X3_A(4,:)=X3_A_042_SpecData_1.data;
%
load('C:\Users\46737\Desktop\Examensarbete\Mätningar\David J
\X3_A_043_Spec.Data 1.mat')
%full text shown here
%C:\Users\46737\Desktop\Examensarbete\Mätningar\David J\
%  X3_A_043_Spec.Data 1.mat
X3_A(5,:)=X3_A_043_SpecData_1.data;
```

4

Figure E.4

```
%
%
load('C:\Users\46737\Desktop\Examensarbete\Mätningar\David J
\X3_BA_044_Spec.Data 1.mat')
%full text shown here
%C:\Users\46737\Desktop\Examensarbete\Mätningar\David J\
%  X3_BA_044_Spec.Data 1.mat
X3_B(1,:)=X3_A_044_SpecData_1.data;
%
load('C:\Users\46737\Desktop\Examensarbete\Mätningar\David J
\X3_B_045_Spec.Data 1.mat')
%full text shown here
%C:\Users\46737\Desktop\Examensarbete\Mätningar\David J\
%  X3_B_045_Spec.Data 1.mat
X3_B(2,:)=X3_B_045_SpecData_1.data;
%
load('C:\Users\46737\Desktop\Examensarbete\Mätningar\David J
\X3_B_046_Spec.Data 1.mat')
%full text shown here
%C:\Users\46737\Desktop\Examensarbete\Mätningar\David J\
%  X3_B_046_Spec.Data 1.mat
X3_B(3,:)=X3_B_046_SpecData_1.data;
%
load('C:\Users\46737\Desktop\Examensarbete\Mätningar\David J
\X3_B_047_Spec.Data 1.mat')
%full text shown here
%C:\Users\46737\Desktop\Examensarbete\Mätningar\David J\
%  X3_B_047_Spec.Data 1.mat
X3_B(4,:)=X3_B_047_SpecData_1.data;
%
load('C:\Users\46737\Desktop\Examensarbete\Mätningar\David J
\X3_B_048_Spec.Data 1.mat')
%full text shown here
%C:\Users\46737\Desktop\Examensarbete\Mätningar\David J\
%  X3_B_048_Spec.Data 1.mat
X3_B(5,:)=X3_B_048_SpecData_1.data;
%
M_X3=[X3_A; X3_B];
%
for i=1:1:10
    hold on
    plot(x_axis+50,M_X3(i,:));
end
axis([0 inf 600 1050])
saveas(gcf,'s_X3.png')
clf

load('C:\Users\46737\Desktop\Examensarbete\Mätningar\David J
\X4_A_025_Spec.Data 1.mat')
%full text shown here
%C:\Users\46737\Desktop\Examensarbete\Mätningar\David J\
%  X4_A_025_Spec.Data 1.mat
X4_A(1,:)=X4_A_025_SpecData_1.data;
%
```


Figure E.5

```
load('C:\Users\46737\Desktop\Examensarbete\Mätningar\David J
\X4_A_026_Spec.Data 1.mat')
%full text shown here
%C:\Users\46737\Desktop\Examensarbete\Mätningar\David J\
%  X4_A_026_Spec.Data 1.mat
X4_A(2,:)=X4_A_026_SpecData_1.data;
%
load('C:\Users\46737\Desktop\Examensarbete\Mätningar\David J
\X4_A_027_Spec.Data 1.mat')
%full text shown here
%C:\Users\46737\Desktop\Examensarbete\Mätningar\David J\
%  X4_A_027_Spec.Data 1.mat
X4_A(3,:)=X4_A_027_SpecData_1.data;
%
load('C:\Users\46737\Desktop\Examensarbete\Mätningar\David J
\X4_A_028_Spec.Data 1.mat')
%full text shown here
%C:\Users\46737\Desktop\Examensarbete\Mätningar\David J\
%  X4_A_028_Spec.Data 1.mat
X4_A(4,:)=X4_A_028_SpecData_1.data;
%
load('C:\Users\46737\Desktop\Examensarbete\Mätningar\David J
\X4_A_029_Spec.Data 1.mat')
%full text shown here
%C:\Users\46737\Desktop\Examensarbete\Mätningar\David J\
%  X4_A_029_Spec.Data 1.mat
X4_A(5,:)=X4_A_029_SpecData_1.data;
%
%
load('C:\Users\46737\Desktop\Examensarbete\Mätningar\David J
\X4_B_030_Spec.Data 1.mat')
%full text shown here
%C:\Users\46737\Desktop\Examensarbete\Mätningar\David J\
%  X4_B_030_Spec.Data 1.mat
X4_B(1,:)=X4_B_030_SpecData_1.data;
%
load('C:\Users\46737\Desktop\Examensarbete\Mätningar\David J
\X4_B_031_Spec.Data 1.mat')
%full text shown here
%C:\Users\46737\Desktop\Examensarbete\Mätningar\David J\
%  X4_B_031_Spec.Data 1.mat
X4_B(2,:)=X4_B_031_SpecData_1.data;
%
load('C:\Users\46737\Desktop\Examensarbete\Mätningar\David J
\X4_B_033_Spec.Data 1.mat')
%full text shown here
%C:\Users\46737\Desktop\Examensarbete\Mätningar\David J\
%  X4_B_033_Spec.Data 1.mat
X4_B(3,:)=X4_B_033_SpecData_1.data;
%
load('C:\Users\46737\Desktop\Examensarbete\Mätningar\David J
\X4_B_034_Spec.Data 1.mat')
%full text shown here
%C:\Users\46737\Desktop\Examensarbete\Mätningar\David J\
```

6

Figure E.6

```
%  X4_B_034_Spec.Data 1.mat
X4_B(4,:)=X4_B_034_SpecData_1.data;
%
load('C:\Users\46737\Desktop\Examensarbete\Mätningar\David J
\X4_B_035_Spec.Data 1.mat')
%full text shown here
%C:\Users\46737\Desktop\Examensarbete\Mätningar\David J\
%  X4_B_035_Spec.Data 1.mat
X4_B(5,:)=X4_B_035_SpecData_1.data;
%
M_X4=[X4_A; X4_B];
%
for i=1:1:10
    hold on
    plot(x_axis+50,M_X4(i,:));
end
axis([0 inf 600 1050])
saveas(gcf,'s_X4.png')
clf

load('C:\Users\46737\Desktop\Examensarbete\Mätningar\David J
\X5_A_004_Spec.Data 1.mat')
%full text shown here
%C:\Users\46737\Desktop\Examensarbete\Mätningar\David J\
%  X5_A_004_Spec.Data 1.mat
X5_A(1,:)=X5_A_004_SpecData_1.data;
%
load('C:\Users\46737\Desktop\Examensarbete\Mätningar\David J
\X5_A_005_Spec.Data 1.mat')
%full text shown here
%C:\Users\46737\Desktop\Examensarbete\Mätningar\David J\
%  X5_A_005_Spec.Data 1.mat
X5_A(2,:)=X5_A_005_SpecData_1.data;
%
load('C:\Users\46737\Desktop\Examensarbete\Mätningar\David J
\X5_A_006_Spec.Data 1.mat')
%full text shown here
%C:\Users\46737\Desktop\Examensarbete\Mätningar\David J\
%  X5_A_006_Spec.Data 1.mat
X5_A(3,:)=X5_A_006_SpecData_1.data;
%
load('C:\Users\46737\Desktop\Examensarbete\Mätningar\David J
\X5_A_007_Spec.Data 1.mat')
%full text shown here
%C:\Users\46737\Desktop\Examensarbete\Mätningar\David J\
%  X5_A_007_Spec.Data 1.mat
X5_A(4,:)=X5_A_007_SpecData_1.data;
%
load('C:\Users\46737\Desktop\Examensarbete\Mätningar\David J
\X5_A_008_Spec.Data 1.mat')
%full text shown here
%C:\Users\46737\Desktop\Examensarbete\Mätningar\David J\
%  X5_A_008_Spec.Data 1.mat
X5_A(5,:)=X5_A_008_SpecData_1.data;
```

7

Figure E.7

```
%
%
load('C:\Users\46737\Desktop\Examensarbete\Mätningar\David J
\X5_B_012_Spec.Data 1.mat')
%full text shown here
%C:\Users\46737\Desktop\Examensarbete\Mätningar\David J\
%  X5_B_012_Spec.Data 1.mat
X5_B(1,:)=X5_B_012_SpecData_1.data;
%
load('C:\Users\46737\Desktop\Examensarbete\Mätningar\David J
\X5_B_013_Spec.Data 1.mat')
%full text shown here
%C:\Users\46737\Desktop\Examensarbete\Mätningar\David J\
%  X5_B_013_Spec.Data 1.mat
X5_B(2,:)=X5_B_013_SpecData_1.data;
%
load('C:\Users\46737\Desktop\Examensarbete\Mätningar\David J
\X5_B_015_Spec.Data 1.mat')
%full text shown here
%C:\Users\46737\Desktop\Examensarbete\Mätningar\David J\
%  X5_B_015_Spec.Data 1.mat
X5_B(3,:)=X5_B_015_SpecData_1.data;
%
load('C:\Users\46737\Desktop\Examensarbete\Mätningar\David J
\X5_B_019_Spec.Data 1.mat')
%full text shown here
%C:\Users\46737\Desktop\Examensarbete\Mätningar\David J\
%  X5_B_019_Spec.Data 1.mat
X5_B(4,:)=X5_B_019_SpecData_1.data;
%
load('C:\Users\46737\Desktop\Examensarbete\Mätningar\David J
\X5_B_020_Spec.Data 1.mat')
%full text shown here
%C:\Users\46737\Desktop\Examensarbete\Mätningar\David J\
%  X5_B_020_Spec.Data 1.mat
X5_B(5,:)=X5_B_020_SpecData_1.data;
%
M_X5=[X5_A; X5_B];
%
for i=1:1:10
    hold on
    plot(x_axis+50,M_X5(i,:));
end
axis([0 inf 600 1050])
saveas(gcf,'s_X5.png')
clf

M_X1_mean=mean(M_X1);
M_X2_mean=mean(M_X2);
M_X3_mean=mean(M_X3);
M_X4_mean=mean(M_X4);
M_X5_mean=mean(M_X5);
plot(x_axis,M_X1_mean,x_axis+50,M_X5_mean,x_axis+50,M_X4_mean,x_axis
+...
```

8

Figure E.8

```
    50,M_X3_mean,x_axis,M_X2_mean);
axis([0 3500 600 850])
legend('A','B','C','D','E')
saveas(gcf,'mean_graphs.png')
clf
%
plot(x_axis,M_X1_mean,x_axis+50,M_X5_mean,x_axis+50,M_X4_mean,x_axis
+...
    50,M_X3_mean,x_axis,M_X2_mean,'LineWidth',1.5);
axis([1200 1750 720 850])
legend('A','B','C','D','E')
saveas(gcf,'mean_graphs_Peaks.png')
clf
%
plot(x_axis,M_X1_mean);
axis([0 inf 600 950])
saveas(gcf,'mean_X1.png')
clf
%
plot(x_axis,M_X2_mean);
axis([0 inf 600 950])
saveas(gcf,'mean_X2.png')
clf
%
plot(x_axis,M_X3_mean);
axis([0 inf 600 950])
saveas(gcf,'mean_X3.png')
clf
%
plot(x_axis,M_X4_mean);
axis([0 inf 600 950])
saveas(gcf,'mean_X4.png')
clf
%
plot(x_axis,M_X5_mean);
axis([0 inf 600 950])
saveas(gcf,'mean_X5.png')
clf

pos1_left=find(x_axis==x_axis(938));
pos1_right=find(x_axis==x_axis(954));
pos2_left=find(x_axis==x_axis(535));
pos2_right=find(x_axis==x_axis(614));
pos3_left=find(x_axis==x_axis(615));
pos3_right=find(x_axis==x_axis(738));
%
for i=1:10
    pos1_max_X1(i,1)=max(M_X1(i,pos1_left:pos1_right));
    pos1_max_X2(i,1)=max(M_X2(i,pos1_left:pos1_right));
    pos1_max_X3(i,1)=max(M_X3(i,pos1_left:pos1_right));
    pos1_max_X4(i,1)=max(M_X4(i,pos1_left:pos1_right));
    pos1_max_X5(i,1)=max(M_X5(i,pos1_left:pos1_right));
    %
    pos2_max_X1(i,1)=max(M_X1(i,pos2_left:pos2_right));
```

9

Figure E.9

```
        pos2_max_X2(i,1)=max(M_X2(i,pos2_left:pos2_right));
        pos2_max_X3(i,1)=max(M_X3(i,pos2_left:pos2_right));
        pos2_max_X4(i,1)=max(M_X4(i,pos2_left:pos2_right));
        pos2_max_X5(i,1)=max(M_X5(i,pos2_left:pos2_right));
        %
        pos3_max_X1(i,1)=max(M_X1(i,pos3_left:pos3_right));
        pos3_max_X2(i,1)=max(M_X2(i,pos3_left:pos3_right));
        pos3_max_X3(i,1)=max(M_X3(i,pos3_left:pos3_right));
        pos3_max_X4(i,1)=max(M_X4(i,pos3_left:pos3_right));
        pos3_max_X5(i,1)=max(M_X5(i,pos3_left:pos3_right));
    end
    factor_peaks_X1=(pos2_max_X1-pos1_max_X1)./(pos3_max_X1-pos1_max_X1);
    factor_peaks_X2=(pos2_max_X2-pos1_max_X2)./(pos3_max_X2-pos1_max_X2);
    factor_peaks_X3=(pos2_max_X3-pos1_max_X3)./(pos3_max_X3-pos1_max_X3);
    factor_peaks_X4=(pos2_max_X4-pos1_max_X4)./(pos3_max_X4-pos1_max_X4);
    factor_peaks_X5=(pos2_max_X5-pos1_max_X5)./(pos3_max_X5-pos1_max_X5);
    %
    X1_factors_sorted=sort(factor_peaks_X1);
    X2_factors_sorted=sort(factor_peaks_X2);
    X3_factors_sorted=sort(factor_peaks_X3);
    X4_factors_sorted=sort(factor_peaks_X4);
    X5_factors_sorted=sort(factor_peaks_X5);
    MeanPF_X1=mean(factor_peaks_X1);
    MeanPF_X2=mean(factor_peaks_X2);
    MeanPF_X3=mean(factor_peaks_X3);
    MeanPF_X4=mean(factor_peaks_X4);
    MeanPF_X5=mean(factor_peaks_X5);
    %
    MaxPF_X1=max(factor_peaks_X1);
    MinPF_X1=min(factor_peaks_X1);
    MaxPF_X2=max(factor_peaks_X2);
    MinPF_X2=min(factor_peaks_X2);
    MaxPF_X3=max(factor_peaks_X3);
    MinPF_X3=min(factor_peaks_X3);
    MaxPF_X4=max(factor_peaks_X4);
    MinPF_X4=min(factor_peaks_X4);
    MaxPF_X5=max(factor_peaks_X5);
    MinPF_X5=min(factor_peaks_X5);
    %
    hold on
    line([0 0],[MaxPF_X1
     MinPF_X1],'Marker','.','color','k','Linestyle',':')
    line([2 2],[MaxPF_X5
     MinPF_X5],'Marker','.','color','k','Linestyle',':')
    line([4 4],[MaxPF_X4
     MinPF_X4],'Marker','.','color','k','Linestyle',':')
    line([8 8],[MaxPF_X3
     MinPF_X3],'Marker','.','color','k','Linestyle',':')
    line([20 20],[MaxPF_X2
     MinPF_X2],'Marker','.','color','k','Linestyle',':')
    %
    line([0 0],[X1_factors_sorted(3)
     X1_factors_sorted(8)],'Marker','x',...
        'color','k','Linestyle','-')
```

10

Figure E.10

```
line([2 2],[X5_factors_sorted(3)
 X5_factors_sorted(8)],'Marker','x',...
    'color','k','Linestyle','-')
line([4 4],[X4_factors_sorted(3)
 X4_factors_sorted(8)],'Marker','x',...
    'color','k','Linestyle','-')
line([8 8],[X3_factors_sorted(3)
 X3_factors_sorted(8)],'Marker','x',...
    'color','k','Linestyle','-')
line([20 20],[X2_factors_sorted(3)
 X2_factors_sorted(8)],'Marker','x',...
    'color','k','Linestyle','-')
%
line([-1 21],[1 1],'Marker','none','color','g','Linestyle','-')
%
plot([0 2 4 8 20],[MeanPF_X1 MeanPF_X5 MeanPF_X4 MeanPF_X3
 MeanPF_X2],...
    'Marker','o','color','k','Linestyle','none');
axis([-1 20 0 1.3])
%
p=polyfit([0 2 4 8 20],...
    [MeanPF_X1 MeanPF_X5 MeanPF_X4 MeanPF_X3 MeanPF_X2],1);
line([0 20],[p(2) (p(1)*20+p(2))],'Marker','none','color','r',...
    'Linestyle','-')
saveas(gcf,'fitted_graph.png')
clf
%
%
%
```